Bi-Axis High-Frequency Sinusoidal Injection Based MTPA Control Method for Sensorless IPMSM Drives

Yunhao Yan, Guoqiang Zhang, *Senior Member, IEEE*, Qiwei Wang, *Member, IEEE*, Binxing Li, *Member, IEEE*, Kairan Wang, Gaolin Wang, *Senior Member, IEEE*, and Dianguo Xu, *Fellow, IEEE*

***Abstract*—The cross-saturation effect causes estimated position inaccuracies, making it difficult to achieve satisfactory maximum torque per ampere (MTPA) control for sensorless interior permanent magnet synchronous motor (IPMSM) drives. To reduce the influence of position estimation error on the optimal current vector angle (OCVA) tracking, a novel bi-axis high-frequency (HF) sinusoidal injection based sensorless MTPA control method is proposed. On the basis of analyzing the influence of position estimation error and parameter mismatch on the OCVA error, a bi-axis HF signal injection mechanism in the zero-mutual-inductance and MTPA frames is established to realize the position estimation and the OCVA tracking, respectively. The efficiency optimization operation criterion is constructed by extracting the excited HF current in the MTPA frame. Then the adaptive compensation mechanism of the current vector angle tracking error is designed, so that the MTPA frame finally converges to the desired position. Theoretical analysis of stability, noise sensitivity and dynamic performance shows that the proposed method can reduce adverse effects such as the cross-saturation effect. Finally, the effectiveness of the proposed method is verified on a 2.2-kW IPMSM drive platform, enhancing the precision of MTPA control for sensorless IPMSM drives.**

***Index Terms*—Bi-axis injection, cross-saturation effect, high-frequency signal injection (HFSI), interior permanent magnet synchronous motor (IPMSM), maximum torque per ampere (MTPA), position estimation error.**

I. Introduction

THE widespread use of inefficient motors causes waste of electricity and high carbon emissions. Permanent magnet synchronous motor (PMSM) has become crucial for enhancing the energy efficiency of motor drive systems due to its high power density and efficiency, including interior PMSM (IPMSM) and surface-mounted PMSM [1], [2], [3]. To reduce system cost and size, improve reliability in harsh environments, position sensorless control has received extensive attention. In addition, the maximum torque per ampere (MTPA) control has become an important way to improve motor efficiency by optimizing the current vector angle [4], [5].

Currently, MTPA control can be broadly categorized into four types, including the analytic calculation-based method, the look-up table (LUT)-based method, the extremum seeking-based method, and the power-perturbation-based method [6]. The analytic calculation-based method calculates the optimal current vector angle (OCVA) by motor model, which involves complex math operations, increasing computational burden and is sensitive to motor parameters [7]. The LUT-based method obtains the OVCA with offline measurements, affecting the generalizability [8]. The extremum seeking-based method adjusts the current vector angle in fixed or variable steps to obtain the OVCA, the stability and dynamic performance under complex conditions need to be improved [9]. The power-perturbation-based method injects actual or virtual high-frequency (HF) signals to obtain the OCVA by constructing the MTPA criterion using the extracted power perturbation [10], [11], [12], [13], [14], [15]. In [13], the influence of the inductance nonlinearity on the MTPA control accuracy was reduced by establishing an offline inductance parameter table. In [14], the feedforward decoupling compensation was proposed to correct the error between the nominal and actual values of the inductance and permanent magnet flux. Both in [13] and [14], the cross-saturation effect is not considered. In [15], a virtual signal injection method with offline parameters was proposed to mitigate the cross-saturation effect for accurate MTPA control. In this method, the dependence of offline parameters needs to be reduced to enhance the generalizability. Therefore, further studies on the influence of the inductance nonlinearity and the cross-saturation effect are needed to improve the MTPA control accuracy.

On the other hand, the MTPA control is affected by the position estimation error in sensorless IPMSM drives. In the medium- and high-speed region, the back electromotive force or flux linkage observers were designed to estimate position. In zero- and low-speed region, the HF signal injection (HFSI) method has been widely used due to its robustness. Despite the low parameter dependence of HFSI method, the cross-saturation effect can still cause position estimation error [16]. To further enhance the performance of HFSI method, some scholars have proposed position estimation error suppression methods, mainly including the offline and online compensation [17], [18], [19]. The above methods can suppress the position estimation

Received 25 June 2025; revised 30 August 2025 and 25 October 2025; accepted 2 November 2025. Date of publication 10 November 2025; date of current version 19 January 2026. This work was supported by the Research Fund for the National Natural Science Foundation of China under Grant 52522703, Grant 52577041, and Grant 52125701. Recommended for publication by Associate Editor Y.-M. Chen. *(Corresponding author: Guoqiang Zhang.)*

The authors are with the School of Electrical Engineering and Automation, Harbin Institute of Technology, Harbin 150001, China. (e-mail: 25b306011@stu.hit.edu.cn; zhgq@hit.edu.cn; wqwhit@hit.edu.cn; lbx@hit.edu.cn; 24b306010@stu.hit.edu.cn; wgl818@hit.edu.cn; xudiang@hit.edu.cn).

Color versions of one or more figures in this article are available at https://doi.org/10.1109/TPEL.2025.3630813.

Digital Object Identifier 10.1109/TPEL.2025.3630813

error caused by the cross-saturation effect. However, additional suppression algorithms increase the complexity of the control system. In addition, MTPA control affected by motor parameters should be considered.

Position estimation error and inductance nonlinearity reduce the accuracy of MTPA control in sensorless IPMSM drives, which have been investigated. In [20], an HF square wave signal was injected to realize both sensorless and MTPA control by demodulating and eliminating some components of the excited current. In this method, the cross-saturation effect is not considered. In [21], based on the active flux model, the virtual q-axis inductance was constructed and adjusted to obtain the OCVA. This method is only available for the medium- and high-speed region. In [22], the adaptive projection vector was used to estimate rotor position and the optimal reference current for MTPA conditions was designed considering parameter mismatch to achieve precise torque control. This method achieves excellent results in the medium- and high-speed region, and the performance in the low-speed region needs to be improved. In [23], the current vector frame was constructed by overlapping the estimated q-axis with the current vector. The dynamic inductance was estimated by injecting pulsating voltage signals and a frequency-adaptive flux observer was designed to obtain the stator flux information. Then the MTPA criterion can be calculated to obtain the OCVA. Due to the use of frequency-adaptive flux observer, this method is limited to the low-speed region. In [24], an MTPA control method for low-speed operation was proposed based on [23]. However, this method requires offline commissioning parameters. In [25], the transient response current slopes of the fundamental maximum active-voltage vector were utilized to splice a specific second harmonic signal containing the OCVA information. Due to the need of sampling the current slopes of the active- and zero-voltage vectors during the PWM cycle, a higher accuracy current sampler is required. For sensorless IPMSM drives, further research is needed to realize the accurate tracking of the OCVA in the presence of the position estimation error and the inductance nonlinearity.

In this article, a novel bi-axis HF sinusoidal injection based sensorless MTPA control method is proposed to improve the OCVA tracking accuracy under the position estimation error. First, the influence of position estimation error and parameter mismatch on the OCVA tracking error is analyzed. To realize the position estimation and the OCVA tracking, a bi-axis HFSI mechanism in the zero-mutual-inductance and MTPA frames is investigated. In the proposed method, the torque equation and the efficiency optimization operation criterion construction approach are analyzed in the presence of position estimation error. And the control criterion in the MTPA frame is established with the extracted excited HF current, so as to reduce the dependence on the motor parameters. To lead the MTPA frame finally converge to the optimal current vector frame, the OCVA tracking error adaptive compensation algorithm is designed by utilizing the reconstructed efficiency optimization operation criterion. Furthermore, a detailed theoretical analysis is carried out in terms of stability and dynamic performance. Finally, the experiments show the effectiveness of the proposed method on a 2.2-kW IPMSM drive platform.

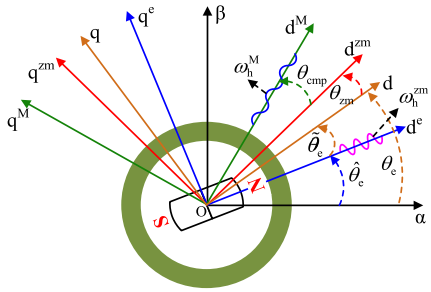

Fig. 1. Reference frames of sensorless IPMSM drives.

II. Analysis of OCVA Tracking Error in Sensorless Controlled IPMSM Drives

A. Position Estimation Based on HFSI Method

Fig. 1 illustrates the reference frames used to analyze the HFSI based position estimation method for sensorless IPMSM drives. α–β, d–q, d^e–q^e, d^{zm}-q^{zm}, and d^M-q^M frames denote the stationary frame, the rotary frame, the estimated frame, the zero-mutual-inductance frame, and MTPA frame, respectively. The zero-mutual-inductance frame is newly defined to describe the frame with a special position related to the cross-saturation effect. In this frame, the mutual-inductance is zero in the mathematical expression, but the cross-saturation effect does not disappear. The MTPA frame coincides with the current vector. ω_e and $\hat{\omega}_e$ are the actual and estimated speeds, respectively. θ_e, $\hat{\theta}_e$, and $\tilde{\theta}_e$ denote the actual position, the estimated position and the position estimation error, respectively, and $\tilde{\theta}_e = \theta_e - \hat{\theta}_e$. The variables in the estimated frame are distinguished by the superscript "e." Similarly, the variables in the zero-mutual-inductance frame and MTPA frame are superscripted with "zm" and "M", respectively.

The HF mathematical model of IPMSM in the d^e-q^e axes can be expressed as

$$\boldsymbol{u}^{\mathbf{e}}_{\mathbf{dqh}} = \boldsymbol{u}_{\mathbf{h}} = \mathrm{e}^{\tilde{\theta}_e \boldsymbol{J}} \boldsymbol{L}_{\mathbf{dq}} \mathrm{e}^{-\tilde{\theta}_e \boldsymbol{J}} \cdot \mathrm{p}\boldsymbol{i}^{\mathbf{e}}_{\mathbf{dqh}} \tag{1}$$

where $\boldsymbol{u}^{\mathbf{e}}_{\mathbf{dqh}} = [u^e_{dh},\ u^e_{qh}]^T$ and $\boldsymbol{i}^{\mathbf{e}}_{\mathbf{dqh}} = [i^e_{dh},\ i^e_{qh}]^T$ are the d^e–q^e axis HF voltage and current vectors, respectively. $\boldsymbol{u}_{\mathbf{h}} = [U_h \cos(\omega_h t),\ 0]^T$ is the injected HF voltage vector, where U_h and ω_h are voltage amplitude and injection frequency, respectively. $\boldsymbol{L}_{\mathbf{dq}} = [L_d,\ L_{dq};\ L_q,\ L_{qd}]$ is the d–q axis inductance matrix, where L_{dq} and L_{qd} are mutual-inductances, and $L_{dq} = L_{qd}$. $\boldsymbol{J} = [0\ -1;\ 10]$ is the orthogonal matrix. p is the differential operator.

From (1), the HF current in the d^e-q^e axes can be obtained as

$$\begin{aligned}\begin{bmatrix} i^e_{dh} \\ i^e_{qh} \end{bmatrix} &= \frac{\int U_h \cos(\omega_h t)dt}{\left(L_d L_q - L^2_{dq}\right)} \begin{bmatrix} L_0 - L_1 \cos\left(2\tilde{\theta}_e\right) + L_{dq} \sin\left(2\tilde{\theta}_e\right) \\ -L_1 \sin\left(2\tilde{\theta}_e\right) - L_{dq} \cos\left(2\tilde{\theta}_e\right) \end{bmatrix} \\ &= \frac{U_h \sin(\omega_h t)}{\omega_h \left(L_d L_q - L^2_{dq}\right)} \begin{bmatrix} L_0 - L_1 \cos\left(2\tilde{\theta}_e\right) + L_{dq} \sin\left(2\tilde{\theta}_e\right) \\ -L_1 \sin\left(2\tilde{\theta}_e\right) - L_{dq} \cos\left(2\tilde{\theta}_e\right) \end{bmatrix}\end{aligned} \tag{2}$$

where L_0 and L_1 are the average and the difference inductances, respectively, which are defined as $L_0 = (L_d + L_q)/2$ and $L_1 = (L_d - L_q)/2$.

The HF current amplitudes can be obtained from the extracted HF current with a demodulation algorithm as

$$\begin{aligned}\begin{bmatrix} I_{dh}^e \\ I_{qh}^e \end{bmatrix} &= \mathrm{LPF}\left(\begin{bmatrix} i_{dh}^e \\ i_{qh}^e \end{bmatrix} \cdot \sin(\omega_h t)\right) \\ &= \frac{U_h}{2\omega_h\left(L_d L_q - L_{dq}^2\right)} \begin{bmatrix} L_0 - L_1\cos\left(2\tilde{\theta}_e\right) + L_{dq}\sin\left(2\tilde{\theta}_e\right) \\ -L_1\sin\left(2\tilde{\theta}_e\right) - L_{dq}\cos\left(2\tilde{\theta}_e\right) \end{bmatrix}\end{aligned} \tag{3}$$

where I_{dh}^e and I_{qh}^e are the d^e–q^e axis HF current amplitudes, respectively. LPF represents the low-pass filter.

From (3), the q^e-axis HF current amplitude contains position error information, thus, the position tracking error ε can be obtained as

$$\begin{aligned}\varepsilon &= \frac{I_{qh}^e}{\sqrt{{I_{dh}^e}^2 + {I_{qh}^e}^2}} \\ &= \frac{\sqrt{{L_1}^2 + {L_{dq}}^2}\cdot\sin\left(2\left(\tilde{\theta}_e + \theta_{zm}\right)\right)}{\sqrt{{L_q}^2 + {L_{dq}}^2 + 2L_0L_1\left(1-\cos\left(2\tilde{\theta}_e\right)\right) + 2L_0L_{dq}\sin\left(2\tilde{\theta}_e\right)}}\end{aligned} \tag{4}$$

$$\theta_{zm} = \frac{1}{2}\arctan\left(2L_{dq}/\left(L_d - L_q\right)\right) \tag{5}$$

where θ_{zm} is the position estimation error caused by the cross-saturation effect.

Conventionally, the rotor position and speed can be obtained by feeding (4) into a phase-locked loop. However, due to the cross-saturation effect, the estimated position can deviate from the actual position by θ_{zm} [26]. The severe cross-saturation effect can even affect the stability of the sensorless control. For ease of description, this deviated reference frame d^{zm}-q^{zm}, which incorporates errors caused by the cross-saturation effect, is called the zero-mutual-inductance frame.

In the zero-mutual-inductance frame, q^e-axis HF current amplitude can be expressed as

$$\begin{aligned}I_{qh}^e &= \frac{U_h}{2\omega_h\left(L_d L_q - L_{dq}^2\right)}\left(L_1\sin\left(2\theta_{zm}\right) - L_{dq}\cos\left(2\theta_{zm}\right)\right) \\ &= -\frac{U_h}{2\omega_h\left(L_d L_q - L_{dq}^2\right)} L_{dq}^{zm} = 0\end{aligned} \tag{6}$$

where, $\frac{U_h}{2\omega_h\left(L_d L_q - L_{dq}^2\right)} \neq 0$.

Therefore, in the zero-mutual-inductance frame, the mutual inductance is zero in the mathematical expression.

B. Influence of Position Estimation Error and Parameter Mismatch on the OCVA Tracking Error

Due to the presence of position estimation error, there are mismatches between the control parameters and the actual parameters for MTPA control in sensorless controlled IPMSM drives, causing the OCVA tracking error. Considering the position estimation error, the actual inductance matrix and the flux matrix in the d^e–q^e axes are

$$\boldsymbol{L}_{\mathbf{dq}}^{\mathbf{e}} = \mathrm{e}^{\tilde{\theta}_e \boldsymbol{J}}\boldsymbol{L}_{\mathbf{dq}}\mathrm{e}^{-\tilde{\theta}_e \boldsymbol{J}}, \boldsymbol{\psi}_{\mathbf{dqf}}^{\mathbf{e}} = e^{\tilde{\theta}_e \boldsymbol{J}}\boldsymbol{\psi}_{\mathbf{f}} \tag{7}$$

where $\boldsymbol{L}_{\mathbf{dq}}^{\mathbf{e}} = [L_d^e, L_{dq}^e; L_q^e, L_{qd}^e]$ is the d^e–q^e axis inductance matrix. $\boldsymbol{\psi}_{\mathbf{dqf}}^{\mathbf{e}} = [\psi_{df}^e, \psi_{qf}^e]^T$ is the d^e–q^e axis permanent magnet flux. $\psi_{\mathbf{f}} = [\psi_f, 0]^T$ is d–q axis permanent magnet flux.

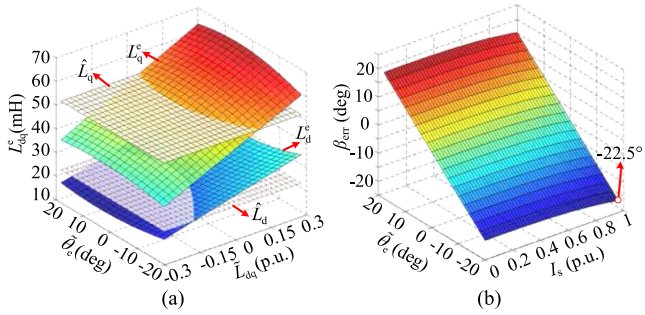

Fig. 2. Inductance parameter and OCVA tracking error when the position estimation error exists. (a) d^e–q^e axis inductance. (b) OCVA tracking error.

On the other hand, L_d, L_q, and L_{dq} vary with load due to the inductance nonlinearity and the cross-saturation effect [27], [28]. Thus, the actual parameters are inconsistent with the nominal parameters, and a relationship exists as

$$\begin{cases}\boldsymbol{L}_{\mathbf{dq}} = \hat{\boldsymbol{L}}_{\mathbf{dq}} + \tilde{\boldsymbol{L}}_{\mathbf{dq}} \\ \boldsymbol{\psi}_{\mathbf{f}} = \hat{\boldsymbol{\psi}}_{\mathbf{f}} + \tilde{\boldsymbol{\psi}}_{\mathbf{f}}\end{cases} \tag{8}$$

where the superscripts "^" and "~" indicate the nominal parameters and the difference between the actual parameters and the nominal parameters, respectively. $\hat{\boldsymbol{L}}_{\mathbf{dq}} = [\hat{L}_d, \hat{L}_{dq}; \hat{L}_q, \hat{L}_{qd}]$ is the d–q axis nominal inductance matrix. $\tilde{\boldsymbol{L}}_{\mathbf{dq}} = [\tilde{L}_d, \tilde{L}_{dq}; \tilde{L}_q, \tilde{L}_{qd}]$ is the d–q axis inductance error matrix. $\hat{\boldsymbol{\psi}}_{\mathbf{f}} = [0, \hat{\psi}_f]^T$ is the d–q axis nominal permanent magnet flux. $\tilde{\boldsymbol{\psi}}_{\mathbf{f}} = [0, \tilde{\psi}_f]^T$ is the error in the d–q axis permanent magnet flux.

Taking the position estimation error, the inductance nonlinearity and the cross-saturation effect into account, the parameter error can be expressed as

$$\begin{cases}\tilde{\boldsymbol{L}}_{\mathbf{dq}}^{\mathbf{e}} = \hat{\boldsymbol{L}}_{\mathbf{dq}} - \boldsymbol{L}_{\mathbf{dq}}^{\mathbf{e}} \\ \tilde{\boldsymbol{\psi}}_{\mathbf{dqf}}^{\mathbf{e}} = \hat{\boldsymbol{\psi}}_{\mathbf{f}} - \boldsymbol{\psi}_{\mathbf{dqf}}^{\mathbf{e}}\end{cases} \tag{9}$$

where $\tilde{\boldsymbol{L}}_{\mathbf{dq}}^{\mathbf{e}} = [\tilde{L}_d^e, \tilde{L}_{dq}^e; \tilde{L}_q^e, \tilde{L}_{qd}^e]$ is the d^e–q^e axis inductance error matrix. $\tilde{\boldsymbol{\psi}}_{\mathbf{dqf}}^{\mathbf{e}} = [\tilde{\psi}_{df}^e, \tilde{\psi}_{qf}^e]^T$ is the error in the d^e–q^e axis permanent magnet flux.

Based on (9), the relationship between the nominal and the d^e–q^e axis parameters is shown in Fig. 2(a). If the nominal parameters are directly used, the performance of sensorless MTPA control will be affected.

As shown in (10), MTPA control is realized by constructing the torque-current partial derivative $dT_e/d\beta_{dq}$ as the MTPA criterion. β_{dq} is the d–q axis OCVA. T_e is the electromagnetic torque. When $dT_e/d\beta_{dq} = 0$, the output torque is maximized at this current vector angle for the same current amplitude, and the motor operates under MTPA conditions

$$\begin{aligned}\frac{dT_e}{d\beta_{dq}} &= \frac{\partial T_e}{\partial i_d}\cdot\frac{di_d}{d\beta_{dq}} + \frac{\partial T_e}{\partial i_q}\cdot\frac{di_q}{d\beta_{dq}} \\ &= \frac{3n_p}{2}\left[\left(L_d - L_q\right)\left({i_d}^2 - {i_q}^2\right) + 4L_{dq}i_d i_q + \psi_f i_d\right]\end{aligned} \tag{10}$$

where n_p is the number of pole pairs. The i_d and i_q are the d–q axis stator currents, respectively.

TABLE I
PARAMETERS OF THE TEST IPMSM

Parameter	Value	Parameter	Value
Rated power	2.2 kW	Phase resistance	1.86 Ω
Rated voltage	380 V	*D*-axis inductance	22 mH
Rated current	4.4 A	*Q*-axis inductance	51 mH
Rated frequency	75 Hz	Pairs of poles	3
Rated torque	14 N·m	Magnetic flux	0.46 Wb

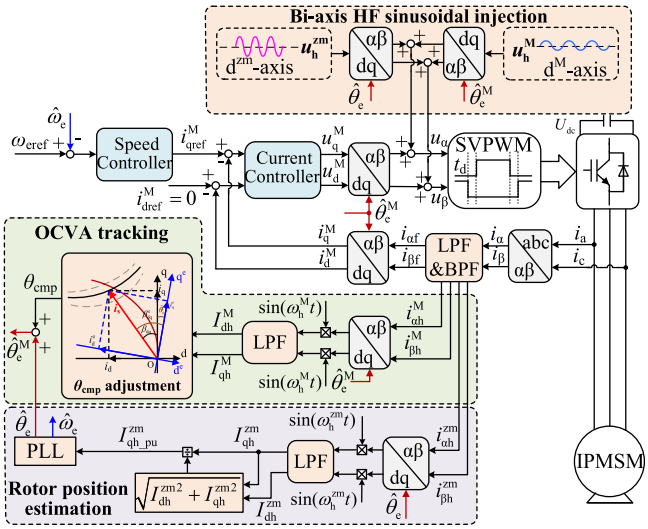

Fig. 3. Block diagram of the proposed bi-axis HF sinusoidal injection based sensorless MTPA control method.

For (10), since it is difficult to obtain the motor parameters accurately, the MTPA criterion constructed from the nominal parameters is not equal to the desired MTPA criterion, affecting the MTPA control accuracy. Fig. 2(b) shows the error between the current vector angle calculated with nominal parameters and the OCVA in the presence of position estimation error. And the motor parameters used are the nominal parameters of the actual motor, as given in Table I. The *d*–*q* axis OCVA is obtained by the extremum seeking-based method when the motor operates with sensor control. The OCVA tracking error $\beta_{\rm err}$ is defined as (11), and as shown in Fig. 2(b), the maximum OCVA tracking error can reach $-22.5°$. Consequently, the position estimation error and parameter mismatch have a large impact on the MTPA control

$$\beta_{err} = (\beta_{dq} + \theta_e) - \left(\beta_{\rm cal} + \hat{\theta}_e\right) \tag{11}$$

where $\beta_{\rm cal}$ is the current vector angle calculated with nominal parameters.

III. Proposed Bi-Axis HF Sinusoidal Injection-Based MTPA Control Method

To achieve effective MTPA control under the position estimation error, the bi-axis HF sinusoidal injection-based method is proposed, as shown in Fig. 3. Two HF sinusoidal signals are injected in the estimated and MTPA frame to realize position estimation and the OCVA tracking, respectively. Unlike the conventional MTPA control method that assigns currents in the

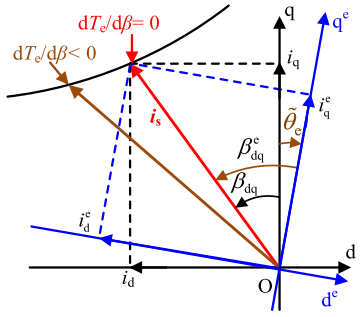

Fig. 4. Relationship of the OCVA under different control frames.

d–*q* axes, this method performs vector control in the MTPA frame. The MTPA frame converges to the optimal current vector frame under the algorithm adjustment to realize the MTPA control. It is worth noting that the proposed method is mainly available in the zero- and low-speed ranges. For higher speed range, a combination of model-based methods and the existing MTPA control methods are needed to achieve MTPA control for sensorless IPMSM drives.

A. MTPA Criterion Construction in Estimated Frame

When motor load is constant, the current vector does not rotate with the rotation of the control frame in steady state. As shown in Fig. 4, the sum of the d^e–q^e axis OCVA β^e_{dq} and the position estimation error $\tilde{\theta}_e$ is equal to the *d*–*q* axis OCVA β_{dq}. Considering the relationship between motor parameters and position estimation error, the expressions of MTPA criterions under different frames are not the same. If the *d*–*q* axis MTPA criterion is used directly, it is difficult to realize accurate MTPA control when the position estimation error exists. The d^e–q^e axis MTPA criterion is constructed in the following.

The d^e–q^e axis steady-state voltage equation and flux equation are shown as

$$\boldsymbol{u}^{\mathbf{e}}_{\mathbf{dq}} = R_{\rm s}\boldsymbol{i}^{\mathbf{e}}_{\mathbf{dq}} + \hat{\omega}_{\rm e}\boldsymbol{J}\boldsymbol{L}^{\mathbf{e}}_{\mathbf{dq}}\boldsymbol{i}^{\mathbf{e}}_{\mathbf{dq}} + \hat{\omega}_{\rm e}\boldsymbol{J}\boldsymbol{\psi}^{\mathbf{e}}_{\mathbf{dqf}} \tag{12}$$

$$\boldsymbol{\psi}^{\mathbf{e}}_{\mathbf{dq}} = \boldsymbol{L}^{\mathbf{e}}_{\mathbf{dq}}\boldsymbol{i}^{\mathbf{e}}_{\mathbf{dq}} + \boldsymbol{\psi}^{\mathbf{e}}_{\mathbf{dqf}} \tag{13}$$

where $\boldsymbol{\psi}^{\mathbf{e}}_{\mathbf{dq}} = [\psi^e_d, \psi^e_q]^T$ is the d^e–q^e axis flux vector. $\boldsymbol{u}^{\mathbf{e}}_{\mathbf{dq}} = [u^e_d, u^e_q]^T$ is the d^e–q^e axis stator voltage vector. $\boldsymbol{i}^{\mathbf{e}}_{\mathbf{dq}} = [i^e_d, i^e_q]^T$ is the d^e–q^e axis stator current vector. R_s is the stator resistance.

From (13), the d^e–q^e axis torque can be expressed as

$$\begin{aligned} T_e &= \frac{3n_{\rm p}}{2}\boldsymbol{i}^{\mathbf{e}}_{\mathbf{dq}}{}^T\boldsymbol{J}\boldsymbol{\psi}^{\mathbf{e}}_{\mathbf{dq}} \\ &= \frac{3n_p}{2}\left[\left(L^e_d - L^e_q\right) i^e_d i^e_q - L^e_{dq}\left(i^{e2}_d - i^{e2}_q\right) + \psi^e_{df} i^e_q - \psi^e_{qf} i^e_d\right]. \end{aligned} \tag{14}$$

Therefore, the d^e–q^e axis MTPA criterion when the position estimation error exists can be obtained as

$$\begin{aligned} \frac{dT_e}{d\beta^e_{dq}} &= \frac{\partial T_e}{\partial i^e_d}\cdot\frac{di^e_d}{d\beta^e_{dq}} + \frac{\partial T_e}{\partial i^e_q}\cdot\frac{di^e_q}{\mathrm{d}\beta^e_{dq}} \\ &= \frac{3n_p}{2}\left[\left(L^e_d - L^e_q\right)\left(i^{e2}_d - i^{e2}_q\right) + 4L^e_{dq} i^e_d i^e_q + \psi^e_{qf} i^e_q + \psi^e_{df} i^e_d\right]. \end{aligned} \tag{15}$$

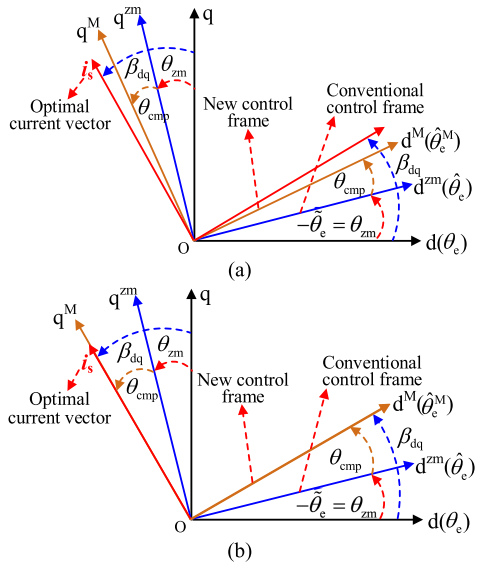

Fig. 5. Control frame adjustment diagram of the proposed method. (a) Before adjustment. (b) After adjustment.

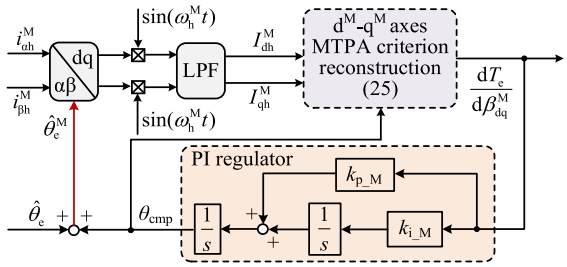

Fig. 6. Adaptive compensation scheme for OCVA tracking error.

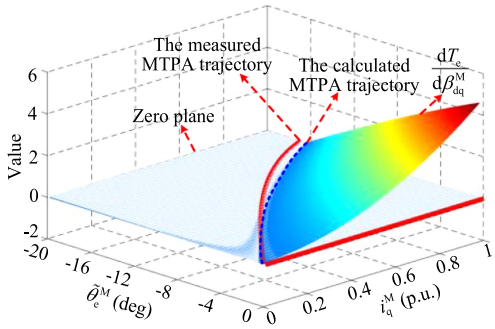

Fig. 7. Value of constructed MTPA criterion.

The general expression for the MTPA criterion in the presence of position estimation error is presented in (15). According to (15), the MTPA criterion in the MTPA frame can be further derived.

Adjusting the d^e–q^e axis MTPA criterion and when $dT_e/d\beta_{dq}^e = 0$, the d^e–q^e axis OCVA can be obtained. Due to the position estimation error and the inductance nonlinearity, the MTPA criterion cannot be accurately obtained, and thus the OCVA cannot be accurately tracked. The conventional position estimation error suppression algorithms could be used. However, it is also difficult to completely eliminate the error, and also the MTPA control is still sensitive to motor parameters.

B. MTPA Control Under Position Estimation Error

From (4), due to the cross-saturation effect, the sensorless control frame eventually converges to the d^{zm}-q^{zm} axes. If the conventional MTPA control is adopted, there will be a deviation between the tracked current vector angle and the OCVA. Thus, the bi-axis HF sinusoidal injection based sensorless MTPA control method is proposed to achieve effective MTPA control. To avoid mutual influence between the two injected HF signals, the injection frequencies are set to be different, and can be expressed as

$$\boldsymbol{u}_{\mathbf{h}}^{\mathbf{zm}} = \begin{bmatrix} U_h^{zm}\cos\left(\omega_h^{zm}t\right) \\ 0 \end{bmatrix}, \quad \boldsymbol{u}_{\mathbf{h}}^{\mathbf{M}} = \begin{bmatrix} U_h^{M}\cos\left(\omega_h^{M}t\right) \\ 0 \end{bmatrix} \tag{16}$$

where $\boldsymbol{u}_{\mathbf{h}}^{\mathbf{zm}}$ and $\boldsymbol{u}_{\mathbf{h}}^{\mathbf{M}}$ are the injected HF voltage vectors for the position estimation and OCVA tracking, respectively. U_h^{zm} and U_h^M are the injected amplitudes. ω_h^{zm} and ω_h^M are the injected frequencies.

Fig. 5 shows the control frame adjustment diagram of the proposed method. The MTPA compensation angle $\theta_{\rm cmp}$ is introduced based on the estimated position to adjust the control frame. In Fig. 5(a), the $\theta_{\rm cmp}$ causes the control frame to approach the optimal current vector frame more closely, but there is still an offset error. As shown in Fig. 5(b), if $\theta_{\rm cmp}$ continues to be adjusted to make $-\tilde{\theta}_e + \theta_{\rm cmp} = \beta_{dq}$ stands, the control frame coincides with the optimal current vector frame, realizing the accurate MTPA control. Therefore, the OCVA tracking error adaptive compensation scheme is designed to obtain the accurate $\theta_{\rm cmp}$, as shown in Fig. 6. To achieve better tracking for ramp inputs, the typical PLL structure is used for MTPA tracking [21], [23]. When applying $i_d^M = 0$, the q^M-axis coincides with the current vector. Since the optimal current vector is unique, the q^M-axis coincides with the optimal current vector frame only when the d^M-q^M axis MTPA criterion is zero. Thus, the d^M-q^M axis MTPA criterion can be combined with the proportional-integral (PI) regulator to realize the adaptive adjustment of $\theta_{\rm cmp}$. Finally, if the q^M-axis coincides with the optimal current vector, the MTPA criterion is equal to zero, and $\theta_{\rm cmp}$ is no longer adjusted, and $\beta_{dq} = \theta_{zm}+\theta_{\rm cmp}$.

When applying $i_d^M = 0$ in the sensorless control, according to (15), the d^M–q^M axis MTPA criterion can be reconstructed as

$$\frac{dT_e}{d\beta_{dq}^M} = -\frac{3n_p}{2}\left[\left(L_d^M - L_q^M\right) i_q^M - \psi_{qf}^M\right] i_q^M \tag{17}$$

where i_q^M is the q^M-axis stator current. L_d^M and L_q^M are the d^M–q^M axis inductances. ψ_{qf}^M is q^M-axis permanent magnet flux.

Fig. 7 shows the value of the constructed d^M–q^M axis MTPA criterion (17). As can be seen from the results, in the area around the calculated MTPA trajectory obtained by the MTPA criterion, the sign of the MTPA criterion is changed. Therefore, the MTPA criterion of the proposed method can be used as the MTPA tracking error signal. Besides, there is a small error between the calculated and the measured MTPA trajectory, which can

be caused by the ignored resistor voltage drop and ignored derivative of machine parameters to current angle [10].

Accurate d^M–q^M axis MTPA criterion is crucial for the proposed method. However, the accurate motor parameters are difficult to obtain. Thus, the HF signal is injected into the d^M–q^M axes to construct the accurate MTPA criterion. Since the frequency of the injected HF signal is much higher than the operating frequency, the resistive voltage drop and the back electromotive force can be neglected. The d^M–q^M axis HF currents can be expressed as

$$\begin{aligned}\begin{bmatrix} i_{dh}^M \\ i_{qh}^M \end{bmatrix} &= \\ \frac{\int U_h^M \cos\left(\omega_h^M t\right)dt}{\left(L_d L_q - L_{dq}^2\right)} &\begin{bmatrix} L_0 - L_1\cos\left(2\tilde{\theta}_e^M\right) + L_{dq}\sin\left(2\tilde{\theta}_e^M\right) \\ -L_1\sin\left(2\tilde{\theta}_e^M\right) - L_{dq}\cos\left(2\tilde{\theta}_e^M\right) \end{bmatrix} \\ = \frac{U_h^M \sin\left(\omega_h^M t\right)}{\omega_h^M\left(L_d L_q - L_{dq}^2\right)} &\begin{bmatrix} L_0 - L_1\cos\left(2\tilde{\theta}_e^M\right) + L_{dq}\sin\left(2\tilde{\theta}_e^M\right) \\ -L_1\sin\left(2\tilde{\theta}_e^M\right) - L_{dq}\cos\left(2\tilde{\theta}_e^M\right) \end{bmatrix}\end{aligned} \tag{18}$$

where i_{dh}^M and i_{qh}^M are the d^M–q^M axis HF currents, respectively. $\tilde{\theta}_e^M$ is the position error between the d^M–q^M axes and the d–q axes, which can be defined as $\tilde{\theta}_e^M = \theta_e - \hat{\theta}_e^M$. In addition, according to Fig. 5, $\tilde{\theta}_e^M = -(\theta_{zm} + \theta_{\rm cmp})$.

The relationship between the d^M–q^M axis and the d^{zm}–q^{zm} axis inductance matrix can be obtained as

$$\begin{aligned}\begin{bmatrix} L_d^M & L_{dq}^M \\ L_{qd}^M & L_q^M \end{bmatrix} &= \mathrm{e}^{-\theta_{\rm cmp}\boldsymbol{J}} \begin{bmatrix} L_d^{zm} & L_{dq}^{zm} \\ L_{qd}^{zm} & L_q^{zm} \end{bmatrix} \mathrm{e}^{\theta_{\rm cmp}\boldsymbol{J}} \\ &= \begin{bmatrix} L_0^{zm} + L_1^{zm}\cos\left(2\theta_{\rm cmp}\right) + L_{dq}^{zm}\sin\left(2\theta_{\rm cmp}\right) \\ \quad - L_1^{zm}\sin\left(2\theta_{\rm cmp}\right) + L_{dq}^{zm}\cos\left(2\theta_{\rm cmp}\right) \\ -L_1^{zm}\sin\left(2\theta_{\rm cmp}\right) + L_{\rm dq}^{\rm zm}\cos\left(2\theta_{\rm cmp}\right) \\ \quad L_0^{zm} - L_1^{zm}\cos\left(2\theta_{\rm cmp}\right) - L_{dq}^{zm}\sin\left(2\theta_{\rm cmp}\right) \end{bmatrix}\end{aligned} \tag{19}$$

where $[L_d^M, L_{dq}^M; L_q^M, L_{qd}^M]$ is the d^M–q^M axis inductance matrix, and $L_{dq}^M = L_{qd}^M$. $[L_d^{zm}, L_{dq}^{zm}; L_q^{zm}, L_{qd}^{zm}]$ is the d^{zm}–q^{zm} axis inductance matrix, and $L_{qd}^{zm} = L_{dq}^{zm} = 0$. $L_0^{zm} = (L_d^{zm} + L_q^{zm})/2$ and $L_1^{zm} = (L_d^{zm} - L_q^{zm})/2$.

The relationship between the d^M–q^M axis and the d–q axis inductance matrix can be obtained as

$$\begin{aligned}\begin{bmatrix} L_d^M & L_{dq}^M \\ L_{qd}^M & L_q^M \end{bmatrix} &= \mathrm{e}^{\tilde{\theta}_e^M\boldsymbol{J}} \begin{bmatrix} L_d & L_{dq} \\ L_{qd} & L_q \end{bmatrix} \mathrm{e}^{-\tilde{\theta}_e^M\boldsymbol{J}} \\ &= \begin{bmatrix} L_0 + L_1\cos\left(2\tilde{\theta}_e^M\right) - L_{dq}\sin\left(2\tilde{\theta}_{\rm e}^{\rm M}\right) \\ \quad L_1\sin\left(2\tilde{\theta}_e^M\right) + L_{dq}\cos\left(2\tilde{\theta}_e^M\right) \\ L_1\sin\left(2\tilde{\theta}_e^M\right) + L_{dq}\cos\left(2\tilde{\theta}_e^M\right) \\ \quad L_0 - L_1\cos\left(2\tilde{\theta}_e^M\right) + L_{dq}\sin\left(2\tilde{\theta}_e^M\right) \end{bmatrix}.\end{aligned} \tag{20}$$

Considering the relationship between the inductance matrices in different frames, as presented in (19) and (20), (18) can be equated as (21), shown at the bottom of this page.

Therefore, the d^M–q^M axis HF current amplitudes can be extracted as

$$\begin{aligned}\begin{bmatrix} I_{dh}^M \\ I_{qh}^M \end{bmatrix} &= \mathrm{LPF}\left(\begin{bmatrix} i_{dh}^M \\ i_{qh}^M \end{bmatrix} \cdot \sin\left(\omega_h^M t\right)\right) \\ &= \frac{U_h^M}{2\omega_h^M\left(L_d^{zm}L_q^{zm} - L_{dq}^{zm2}\right)} \\ &\quad \begin{bmatrix} L_0^{zm} - L_1^{zm}\cos\left(2\theta_{\rm cmp}\right) - L_{dq}^{zm}\sin\left(2\theta_{\rm cmp}\right) \\ \quad L_1^{zm}\sin\left(2\theta_{\rm cmp}\right) - L_{dq}^{zm}\cos\left(2\theta_{\rm cmp}\right) \end{bmatrix}\end{aligned} \tag{22}$$

where I_{dh}^M and I_{qh}^M are the d^M–q^M axis HF current amplitudes, respectively.

Combining the extracted d^M–q^M axis HF current amplitudes with the inductance transformation matrix (19) yields

$$\begin{bmatrix} I_{dh}^M \\ I_{qh}^M \end{bmatrix} = \frac{U_h^M}{2\omega_h^M\left(L_d^{zm}L_q^{zm} - L_{dq}^{zm2}\right)} \begin{bmatrix} L_q^M \\ -L_{dq}^M \end{bmatrix} = k\begin{bmatrix} L_q^M \\ -L_{dq}^M \end{bmatrix} \tag{23}$$

where

$$\begin{aligned} L_d^{zm}L_q^{zm} - L_{dq}^{zm2} &= L_d^M L_q^M - {L_{dq}^M}^2, \\ k &= \frac{U_h^M}{2\omega_h^M\left(L_d^{zm}L_q^{zm} - L_{dq}^{zm2}\right)}. \end{aligned} \tag{24}$$

From (23), kL_q^M and kL_{dq}^M can be obtained from the extracted HF current amplitudes, but k cannot be obtained directly, so it is not possible to directly obtain $L_d^M - L_q^M$. Combined with (19), the relationship between $\theta_{\rm cmp}$ and d^M-q^M axis inductance is

$$\theta_{\rm cmp} = -\frac{1}{2}\arctan\left(\frac{2L_{dq}^M}{L_d^M - L_q^M}\right). \tag{25}$$

Thus, according to (25), L_d^M can be derived as

$$L_d^M = \frac{2L_{dq}^M}{-\tan\left(2\theta_{\rm cmp}\right)} + L_q^M = \frac{2I_{qh}^M}{k\tan\left(2\theta_{\rm cmp}\right)} + \frac{I_{dh}^M}{k}. \tag{26}$$

According to (24) and (26), k can be derived as

$$\begin{aligned} k &= \frac{U_h^M}{2\omega_h^M\left(L_d^{zm}L_q^{zm} - L_{dq}^{\rm zm2}\right)} = \frac{U_h^M}{2\omega_h^M\left(L_d^M L_q^M - {L_{dq}^M}^2\right)} \\ &= \frac{U_{\rm h}^{\rm M}}{2\omega_h^M\left(\left(\frac{2I_{qh}^M}{k\tan(2\theta_{\rm cmp})} + \frac{I_{dh}^M}{k}\right)\frac{I_{dh}^M}{k} - \left(\frac{-I_{qh}^M}{k}\right)^2\right)} \\ &= \frac{k^2 U_{\rm h}^{\rm M}}{2\omega_h^M\left(\left(\frac{2I_{qh}^M}{\tan(2\theta_{\rm cmp})} + I_{dh}^M\right)I_{dh}^M - {I_{qh}^M}^2\right)}. \end{aligned} \tag{27}$$

For expression simplification, define h as

$$h = \frac{2I_{qh}^M}{\tan\left(2\theta_{\rm cmp}\right)} + I_{dh}^M. \tag{28}$$

$$\begin{aligned}\begin{bmatrix} i_{dh}^M \\ i_{qh}^M \end{bmatrix} &= \frac{\int U_h^M\cos\left(\omega_h^M t\right)dt}{\left(L_d^{zm}L_q^{zm} - L_{dq}^{\rm zm2}\right)} \begin{bmatrix} L_0^{zm} - L_1^{zm}\cos\left(2\theta_{\rm cmp}\right) - L_{dq}^{zm}\sin\left(2\theta_{\rm cmp}\right) \\ L_1^{zm}\sin\left(2\theta_{\rm cmp}\right) - L_{dq}^{zm}\cos\left(2\theta_{\rm cmp}\right) \end{bmatrix} \\ &= \frac{U_h^M\sin\left(\omega_h^M t\right)}{\omega_h^M\left(L_d^{zm}L_q^{zm} - L_{dq}^{\rm zm2}\right)} \begin{bmatrix} L_0^{zm} - L_1^{zm}\cos\left(2\theta_{\rm cmp}\right) - L_{dq}^{zm}\sin\left(2\theta_{\rm cmp}\right) \\ L_1^{zm}\sin\left(2\theta_{\rm cmp}\right) - L_{dq}^{zm}\cos\left(2\theta_{\rm cmp}\right) \end{bmatrix}.\end{aligned} \tag{21}$$

Therefore, according to (27) and (28), combine the extracted HF current amplitudes and $\theta_{\rm cmp}$, k can be calculated as

$$k = \frac{2\omega_h^M \left(hI_{dh}^M - {I_{qh}^M}^2\right)}{U_h^M}. \tag{29}$$

On the other hand, since the inductance value correlates with the extracted HF current amplitudes, $L_d^M - L_q^M$ can be derived as

$$\begin{aligned} L_d^M - L_q^M &= \frac{2L_{dq}^M}{-\tan\left(2\theta_{\rm cmp}\right)} = \frac{2I_{qh}^M}{k\tan\left(2\theta_{\rm cmp}\right)} \\ &= \frac{I_{qh}^M U_h^M}{\tan\left(2\theta_{\rm cmp}\right)\omega_h^M\left(hI_{dh}^M - {I_{qh}^M}^2\right)}. \end{aligned} \tag{30}$$

For the d^M–q^M axis voltage equation, when applying $i_d^M = 0$, q^M-axis permanent magnet flux ψ_{qf}^M can be derived as

$$\psi_{qf}^M = -\left(\frac{u_d^M}{\hat{\omega}_e} + L_q^M i_q^M\right) = -\frac{u_d^M}{\hat{\omega}_e} - \frac{U_h^M I_{dh}^M i_q^M}{2\omega_h^M\left(hI_{dh}^M - {I_{qh}^M}^2\right)}. \tag{31}$$

According to (17), (30), and (31), the d^M–q^M axis MTPA criterion can be constructed as (32). It can be seen that the MTPA criterion utilizes only the extracted excited HF current amplitudes, reducing the dependence on motor parameters. $\theta_{\rm cmp}$ can be adaptively adjusted by combining the reconstructed d^M–q^M axis MTPA criterion with the PI regulator. When the q^M-axis coincides with the optimal current vector frame, the MTPA criterion is equal to zero, and $\theta_{\rm cmp}$ no longer changes

$$\frac{dT_e}{d\beta_{dq}^M} = -\frac{3n_p}{2}\left(\frac{hU_h^M i_q^M}{2\omega_h^M\left(hI_{dh}^M - {I_{qh}^M}^2\right)} + \frac{u_d^M}{\hat{\omega}_e}\right) i_q^M. \tag{32}$$

It is noted that the information of ψ_{qf}^M cannot be obtained by (31) when the speed is zero. However, ψ_{qf}^M can be calculated by (7) and (23).

The d^M–q^M axis inductance matrix can be expressed as

$$\boldsymbol{L}_{\mathbf{dq}}^M = {\rm e}^{\tilde{\theta}_e^M \boldsymbol{J}} \boldsymbol{L}_{\mathbf{dq}} {\rm e}^{-\tilde{\theta}_e^M \boldsymbol{J}}. \tag{33}$$

According to (33), L_d^M can be obtained as

$$L_d^M = \frac{2\left(L_q^M\cos\left(2\tilde{\theta}_e^M\right) - L_{dq}^M\sin\left(2\tilde{\theta}_e^M\right) + L_d\right)}{1+\cos\left(2\tilde{\theta}_e^M\right)} - L_q^M. \tag{34}$$

Since the value of L_d^M, L_q^M, and L_{dq}^M can be calculated by the extracted HF current amplitudes, when L_d is considered as a constant value, $\sin(2(\tilde{\theta}_e^M))$ and ψ_{qf}^M can be calculated as

$$\begin{cases} \sin\left(2\left(\tilde{\theta}_e^M\right)\right) = \dfrac{-\sin^2(2\theta_{\rm cmp})\left(kL_d - I_{dh}^M - \frac{I_{qh}^M}{\tan(2\theta_{\rm cmp})}\right)}{I_{qh}^M} \\ \quad + \dfrac{\sin(4\theta_{\rm cmp})\sqrt{kL_d\left(\frac{2I_{qh}^M}{\tan(2\theta_{\rm cmp})} + 2I_{dh}^M - kL_d\right)}}{2I_{qh}^M} \\ \psi_{qf}^M = \psi_f \sin\left(\tilde{\theta}_e^M\right) \end{cases}. \tag{35}$$

Although at zero speed, ψ_{qf}^M is affected by ψ_f and L_d using (35), the d-axis inductance and the permanent magnet flux vary slightly with load, and thus have less effect on the MTPA control [29].

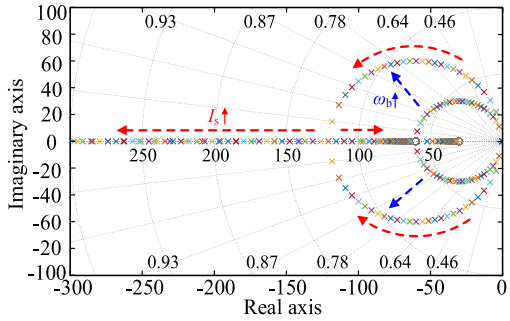

Fig. 8. Zero-pole distribution of the proposed method.

C. Stability Analysis and Parameter Selection

To further prove the stability of the adaptive compensation system for the OCVA tracking error, a small-signal model of $dT_e/d\beta_{dq}^M$ is constructed. Firstly, by linearizing $dT_e/d\beta_{dq}^M$ around $\theta_{\rm cmp}$, (27) can be rewritten as

$$\frac{dT_e}{d\beta_{dq}^M} = m\tilde{\beta} + n \tag{36}$$

where

$$\begin{aligned} m &= 6n_p I_{s0}\left(I_{s0}(L_1\sin(2\beta_{dq}) - L_{dq}\cos(2\beta_{dq})) - \frac{\psi_f\cos\beta_{dq}}{4}\right) \\ n &= -3n_p {I_{s0}}^2\left(L_1\cos\left(2\beta_{dq}\right) + L_{dq}\sin\left(2\beta_{dq}\right)\right) \\ &\quad - \frac{3n_p}{2} I_{s0}\psi_f\sin\beta_{dq} = 0. \end{aligned} \tag{37}$$

In (37), $\tilde{\beta}$ is the small deviation around $\theta_{\rm cmp}$. I_{s0} is the current vector magnitude, which corresponds to the speed loop output value.

For the MTPA control method in Fig. 6, the closed-loop transfer function of the estimated $\theta_{\rm cmp}$ and the d^e–q^e axis OCVA β_{dq}^e can be obtained as

$$\frac{\theta_{\rm cmp}}{\beta_{dq}^e} = \frac{\theta_{\rm cmp}}{\beta_{dq} - \theta_{zm}} = \frac{-m\left(sk_{p\_M} + k_{i\_M}\right)}{s^2 - m\left(sk_{p\_M} + k_{i\_M}\right)} \tag{38}$$

where k_{p_M} and k_{i_M} are the proportional gain and integral gain of the controller, respectively.

To ensure stable convergence of $\theta_{\rm cmp}$, the poles in (38) should be located in the left half of the s-plane. From (37), m is negative, so to ensure the stability of the proposed method, the controller parameters are positive, and for a second-order system, the controller parameters can be designed as

$$\begin{cases} k_{p\_M} = 2\zeta\omega_m \\ k_{i\_M} = {\omega_m}^2 \end{cases} \tag{39}$$

where ω_m is the desired bandwidth and ζ is the damping factor.

Fig. 8 shows the zero-pole distribution of (38), and the parameters are designed according to (39). For the zero-pole plot, it can be seen that there are no zeros and poles located in the right half plane during motor current variation. Therefore, the proposed method is stable when using the parameter design approach in the article.

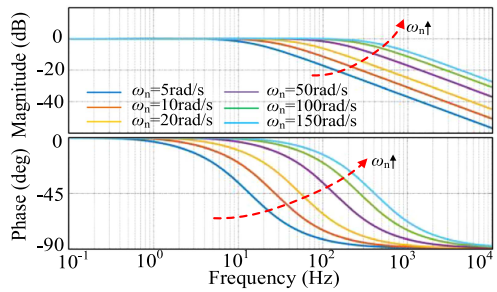

Fig. 9. Effect of ω_m on the noise sensitivity and dynamic performance.

Fig. 9 shows the effect of ω_m on the noise sensitivity and dynamic performance. As the bandwidth increases, the dynamic performance increases, but the noise sensitivity also increases. When choosing the parameters, the noise sensitivity and dynamic performance should be considered comprehensively.

In practical applications, the designed parameters for the proposed method include the injection frequency, the injection magnitude, and the PI control parameters for the adaptive compensation scheme.

Combining (38) and (39), the parameters of the controller can be expressed as

$$\begin{cases} k_{p\_M} = 2\zeta\omega_m = \frac{2\zeta\omega_b}{m} \\ k_{i\_M} = {\omega_m}^2 = \frac{{\omega_b}^2}{m} \end{cases} \tag{40}$$

where ω_b is the desired closed-loop estimation bandwidth.

The PI control parameters and the coefficient m determine the closed-loop estimation bandwidth. To avoid the influence of not eliminating HF signals for position estimation, the closed-loop estimation bandwidth can be chosen to be 1/20-1/10 of the injection frequency (HF signal for position estimation). In addition, the value of m can be calculated approximately at the rated load. And then, according to the designed closed-loop estimation bandwidth, the PI control parameters can be determined.

The proposed sensorless MTPA control requires reducing the impact of injected signals on motor operation while ensuring accurate signal extraction. Thus, the amplitude and frequency of the two injected signals need to be selected [30], [31], [32]. For HF sinusoidal injection schemes, the injection frequency should generally not exceed 1/8 of the carrier frequency. To ensure dynamic performance, since $\boldsymbol{u}_{\mathbf{h}}^{\mathbf{zm}}$ is used to estimate position, the injection frequency of $\boldsymbol{u}_{\mathbf{h}}^{\mathbf{zm}}$ is set higher than $\boldsymbol{u}_{\mathbf{h}}^{\mathbf{M}}$. Meanwhile, to prevent mutual interference between the two injected signals during signal demodulation, as well as to consider the LPF bandwidth in the signal processing process, it is necessary to satisfy

$$\min\left\{2f_h^M, f_h^{zm} - f_h^M\right\} > 10f_{\mathrm{LPF}} \tag{41}$$

where f_h^{zm} is the injection frequency for position estimation, f_h^M is the injection frequency for MTPA criterion construction, and f_{LPF} is the cutoff frequency of the LPF.

Therefore, the selection of the injection frequency for the two signals needs to satisfy

$$\begin{cases} f_h^{zm} \le \frac{1}{8} f_s \\ f_h^{zm} > f_h^M \\ \min\left\{2f_h^M, f_h^{zm} - f_h^M\right\} > 10f_{\mathrm{LPF}} \end{cases} \tag{42}$$

where f_s is the sampling frequency.

The injection amplitude needs to consider both the signal-to-noise ratio (SNR) and the torque ripples. The higher the injection amplitude, the higher the SNR, but also the higher the torque ripples and the lower the available voltage margin. Therefore, the injection amplitude is chosen to be as small as possible while ensuring the SNR. Moreover, for the two HF signals with different frequencies, the injected signal amplitude is generally chosen to be proportional to the injected frequency to maintain a constant amplitude-frequency ratio. According to (3), the amplitude of the HF current is determined by the injected voltage, injection frequency, and inductance. Therefore, the amplitude of the injected voltages can be expressed as

$$\begin{cases} U_h^{zm} = 2\omega_h^{zm} L_d^{zm} \cdot A\% I_{\mathrm{rated}} \\ \frac{U_h^M}{\omega_h^M} = \frac{U_h^{zm}}{\omega_h^{zm}} \end{cases} \tag{43}$$

where the value of $A\%$ typically ranges from 5% to 20% I_{rated} is the rated current of the motor.

When the injected signal frequencies are relatively close, the HF currents at ω_h^{zm} is not completely filtered out for the MTPA criterion construction, and the residual components can be expressed as

$$\begin{bmatrix} i_{dh\_\mathrm{res}}^e \\ i_{qh\_\mathrm{res}}^e \end{bmatrix} = \begin{bmatrix} f_{dh\_\mathrm{res}}^e\left(\tilde{\theta}_e\right) \\ f_{qh\_\mathrm{res}}^e\left(\tilde{\theta}_e\right) \end{bmatrix} \sin\left(\omega_h^{zm} t + \varphi_{dzm}\right) \tag{44}$$

where $i_{dh\_\mathrm{res}}^e$ and $i_{qh\_\mathrm{res}}^e$ are the residual HF currents at ω_h^{zm} that are not completely filtered out. φ_{dzm} is the phase shift introduced from the BPF. $f_{dh\_\mathrm{res}}^e(\tilde{\theta}_e)$ and $f_{qh\_\mathrm{res}}^e(\tilde{\theta}_e)$ are the magnitudes of the HF components after attenuation.

Therefore, the extracted HF currents can be expressed as

$$\begin{aligned} \begin{bmatrix} i_{dh\_\mathrm{BPF}}^M \\ i_{qh\_\mathrm{BPF}}^M \end{bmatrix} &= \begin{bmatrix} f_{dh}^M\left(\tilde{\theta}_e^M\right) \\ f_{qh}^M\left(\tilde{\theta}_e^M\right) \end{bmatrix} \\ &\sin\left(\omega_h^M t\right) + \begin{bmatrix} f_{dh\_\mathrm{res}}^e\left(\tilde{\theta}_e\right) \\ f_{qh\_\mathrm{res}}^e\left(\tilde{\theta}_e\right) \end{bmatrix} \sin\left(\omega_h^{zm} t + \varphi_{dzm}\right) \end{aligned} \tag{45}$$

$$\begin{aligned} &\begin{bmatrix} f_{dh}^M\left(\tilde{\theta}_e^M\right) \\ f_{qh}^M\left(\tilde{\theta}_e^M\right) \end{bmatrix} = \frac{U_h^M}{\omega_h^M\left(L_d L_{\mathrm{q}} - L_{dq}^2\right)} \\ &\begin{bmatrix} L_0 - L_1\cos\left(2\tilde{\theta}_e^M\right) + L_{dq}\sin\left(2\tilde{\theta}_e^M\right) \\ -L_1\sin\left(2\tilde{\theta}_e^M\right) - L_{dq}\cos\left(2\tilde{\theta}_e^M\right) \end{bmatrix} \end{aligned} \tag{46}$$

where $i_{dh\_\mathrm{BPF}}^M$ and $i_{qh\_\mathrm{BPF}}^M$ denote the HF currents obtained through BPF. $f_{dh}^M(\tilde{\theta}_e^M)$ and $f_{qh}^M(\tilde{\theta}_e^M)$ are the magnitude of the HF components for MTPA criterion construction.

And then, through demodulation of the extracted HF signal, the amplitude of the HF currents can be determined and represented as (47), shown at the bottom of the next page. As can be seen from (47), the extracted HF currents after demodulation contain: a dc component; a component at $2\omega_h^M$; a component at $\omega_h^M + \omega_h^{zm}$; and a component at $\omega_h^{zm} - \omega_h^M$.

Additionally, the LPF is typically employed to extract the amplitude of the HF currents for MTPA criterion construction. In designing the LPF, its cutoff frequency is selected to be 1/10

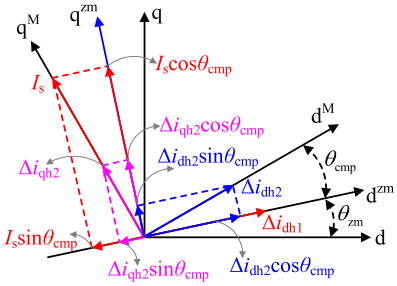

Fig. 10. Current distribution diagram.

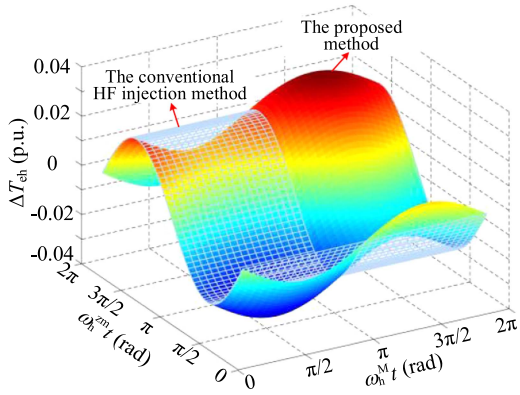

Fig. 11. Analysis of the HF torque ripple.

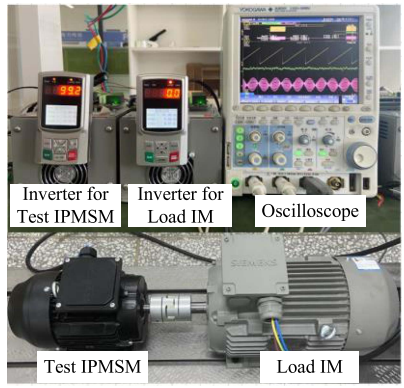

Fig. 12. 2.2-kW IPMSM experimental platform.

of the $\omega_h^{zm} - \omega_h^M$. Consequently, all components except the dc component are filtered out. Therefore, HF current amplitudes can be expressed as

$$\begin{bmatrix} I_{dh}^M \\ I_{qh}^M \end{bmatrix} = \mathrm{LPF}\left(\begin{bmatrix} i_{dh\_\mathrm{BPF}}^M \\ i_{qh\_\mathrm{BPF}}^M \end{bmatrix} \sin\left(\omega_h^M t\right) \right) = \frac{1}{2} \begin{bmatrix} f_{dh}^M\left(\tilde{\theta}_e^M\right) \\ f_{qh}^M\left(\tilde{\theta}_e^M\right) \end{bmatrix}. \tag{48}$$

Likewise, the influence of the residual component at ω_h^M on position estimation follows a similar analytical approach as its effect on the MTPA criterion construction. Therefore, the residual HF components remain after signal extraction, which are effectively filtered out during demodulation. Consequently, these residual components have little impact on both position estimation and MTPA criterion construction.

The proposed method improves MTPA control accuracy in the presence of the position estimation error. However, the injection of two HF signals may introduce additional torque ripple. Fig. 10 shows the current distribution, and the HF torque ripple of the proposed method can be expressed as (49), shown at the bottom of this page. Δi_{dh1} represents the HF current induced by the HF voltage for the position estimation. Δi_{dh2} and Δi_{qh2} denote the HF currents induced by the HF voltage for the OCVA tracking. I_{s} represents the current amplitude.

Fig. 11 presents a comparative analysis of torque ripple between the proposed method and the conventional pulsating injection method. As shown in Fig. 11, the torque ripple of the proposed method is slightly higher than that of the conventional method. Although the proposed method leads to a certain increase in torque ripple, it not only enables the sensorless control system to operate stably under significant cross-saturation effect but also allows the system to maintain MTPA operation.

IV. Experimental Results

The validity and feasibility of the proposed method are verified on a 2.2-kW IPMSM experimental platform, as shown in Fig. 12. The motor parameters are given in Table I, and the PWM carrier frequency is 8 kHz. The test commercial IPMSM and the load induction motor (IM) are coaxially connected, and

$$\begin{aligned} \begin{bmatrix} i_{dh\_\mathrm{BPF}}^M \\ i_{qh\_\mathrm{BPF}}^M \end{bmatrix} \sin\left(\omega_h^M t\right) &= \begin{bmatrix} f_{dh}^M\left(\tilde{\theta}_e^M\right) \\ f_{qh}^M\left(\tilde{\theta}_e^M\right) \end{bmatrix} \sin^2\left(\omega_h^M t\right) + \begin{bmatrix} f_{dh\_\mathrm{res}}^e\left(\tilde{\theta}_e\right) \\ f_{qh\_\mathrm{res}}^e\left(\tilde{\theta}_e\right) \end{bmatrix} \sin\left(\omega_h^{zm} t + \varphi_{dzm}\right) \sin\left(\omega_h^M t\right) \\ &= \begin{bmatrix} f_{dh}^M\left(\tilde{\theta}_e\right) \\ f_{qh}^M\left(\tilde{\theta}_e\right) \end{bmatrix} \frac{1-\cos\left(2\omega_h^M t\right)}{2} + \begin{bmatrix} f_{dh\_\mathrm{res}}^e\left(\tilde{\theta}_e^M\right) \\ f_{qh\_\mathrm{res}}^e\left(\tilde{\theta}_e^M\right) \end{bmatrix} \frac{\cos\left(\left(\omega_h^{zm}-\omega_h^M\right)t+\varphi_{dzm}\right)-\cos\left(\left(\omega_h^{zm}+\omega_h^M\right)t+\varphi_{dzm}\right)}{2} \end{aligned}. \tag{47}$$

$$\begin{aligned} \Delta T_{eh} &= \frac{3n_p}{2}\left(\left(L_d^{zm} - L_q^{zm}\right) i_d^{zm} i_q^{zm} + \psi_{df}^{zm} i_d^{zm} - \psi_{qf}^{zm} i_d^{zm}\right) - T_{\mathrm{e}} \\ &= \frac{3n_p}{2}\left\{ \begin{array}{l} \left(L_d^{zm} - L_q^{zm}\right)\left[\Delta i_{dh2}\Delta i_{qh2}\cos 2\theta_{\mathrm{cmp}} + 0.5\left(\Delta {i_{dh2}}^2 - \Delta {i_{qh2}}^2\right)\sin 2\theta_{\mathrm{cmp}} + \Delta i_{dh1}\left(\Delta i_{dh2}\sin\theta_{\mathrm{cmp}} + \Delta i_{qh2}\cos\theta_{\mathrm{cmp}}\right)\right] \\ +\Delta i_{\mathrm{dh2}}\left[\left(L_d^{zm} - L_q^{zm}\right) I_s\cos 2\theta_{\mathrm{cmp}} + \psi_f \sin\beta_{dq}\right] + \Delta i_{qh2}\left[\psi_f\cos\beta_{dq} - \left(L_d^{zm} - L_q^{zm}\right) I_s \sin 2\theta_{\mathrm{cmp}}\right] \\ +\Delta i_{\mathrm{dh1}}\left[\left(L_d^{zm} - L_q^{zm}\right) I_s\cos\theta_{\mathrm{cmp}} + \psi_f \sin\theta_{zm}\right] \end{array} \right\}. \end{aligned} \tag{49}$$

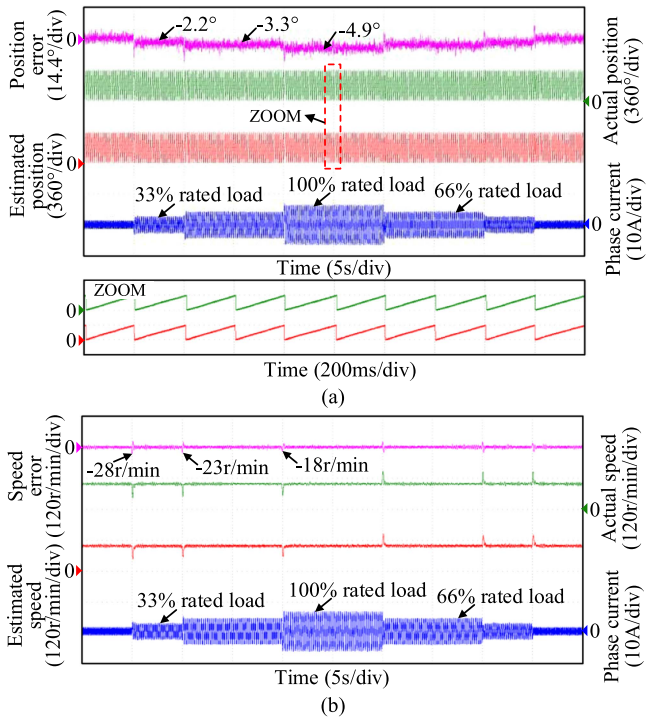

Fig. 13. Experimental results at 100 r/min under continuous load variation conditions with HFSI based method. (a) Position estimation results. (b) Speed estimation results.

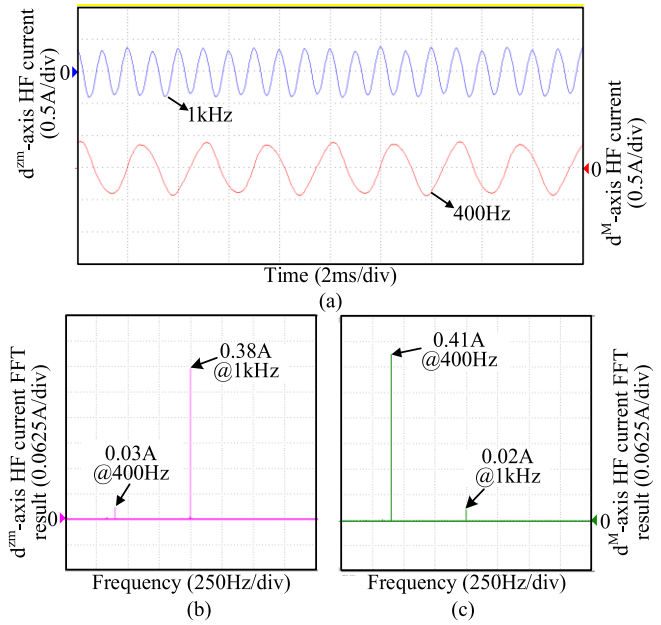

Fig. 14. Extracted excited HF currents. (a) Current waveforms. (b) FFT result of d^{zm}-axis HF current. (c) FFT result of d^{M}-axis HF current.

the load torque is provided by the IM. An incremental encoder with 2000 p/r is applied to detect the actual rotor position only for comparison. The experimental results are provided under different load and speed conditions. The MTPA angle error is defined as shown in (11), and $\beta_{\rm cal}$ is equal to $\theta_{\rm cmp}$ for the proposed method. For the uncompensated method, $\beta_{\rm cal}$ is calculated with the nominal parameters. Since $f_{\rm pwm} = 8$ kHz and the current loop bandwidth is 200 Hz, f_h^{zm} is 1 kHz and f_h^M is 400 Hz for the injected signals, and the injection amplitude U_h^{zm} and U_h^M are 0.15 and 0.06 p.u., respectively. The MTPA control parameters k_{p_M} is 28, and k_{i_M} is 400. To systematically evaluate the performance of the proposed method, the experimental results are organized into three parts: the signal extraction and compensation results, the comparisons under different conditions, and the comprehensive evaluation.

A. Signal Extraction and Compensation Results

First, Fig. 13 shows the experimental results at 100 r/min with continuous load variation conditions with HFSI-based method. In the experiments, only the HFSI-based method is used to estimate the position and speed to realize sensorless control. The position estimation error is the difference between the actual position and the estimated position. From Fig. 13(a), the position errors are −2.2°, −3.3°, and −4.9° at 33%, 66%, and 100% rated load, respectively, which are caused by the cross-saturation effect. From Fig. 13(b), the speed errors are −28 r/min, −23 r/min, and −18 r/min during the transient process when applying 33%, 66%, and 100% rated load, respectively.

Fig. 14 shows the d^{zm}-axis and d^M-axis HF current extracted from the sampled currents using the band-pass filters, and the HF current frequencies are 1 and 400 Hz, respectively. From the FFT result in Fig. 14(b), for the extracted d^{zm}-axis current, the 1 kHz current component is 0.38 A, and the 400 Hz current component is only 0.03 A. Similarly, from the FFT result in Fig. 14(c), for the extracted d^M-axis current, the 400 Hz current component is 0.41 A, while the 1 kHz current component is only 0.02 A. Thus, the two HF signals can be extracted separately to realize position estimation and the OCVA tracking. It is noted that the output of the experimental results is through the DAC channel of the controller. The output waveform from the DAC channel is displayed on the oscilloscope, with the oscilloscope's interpolation set to "Sine" mode. What's more, since the injection frequencies of the two signals are not the same, their injection amplitudes are set according to the principle of ensuring that the amplitudes of the excited HF currents are essentially the same. As a result, the extracted current amplitudes are essentially the same. The frequency-to-amplitude ratio and the q-axis inductance determine the amplitude of the response current. Despite the injection frequencies of the two signals not being the same, their frequency-to-amplitude ratios are set to be the same. What's more, since the misalignment angle of the d^M–q^M axes is larger than that of the d^{zm}–q^{zm} axes, L_q^M is smaller than L_q^{zm}. Thus, the amplitude of the 400 Hz signal is smaller than that of the 1 kHz signal. However, limited by the DAC bandwidth, the amplitude attenuation of the 1 kHz output signal is larger. As a result, the extracted current amplitude at 1 kHz is slightly smaller than that at 400 Hz.

Fig. 15 shows the experimental comparison before and after enabling the proposed method under rated load at 100 r/min. When the algorithm is not enabled, $\beta_{\rm cal}$ is set to zero. From the results, it can be seen that the MTPA angle error is initially

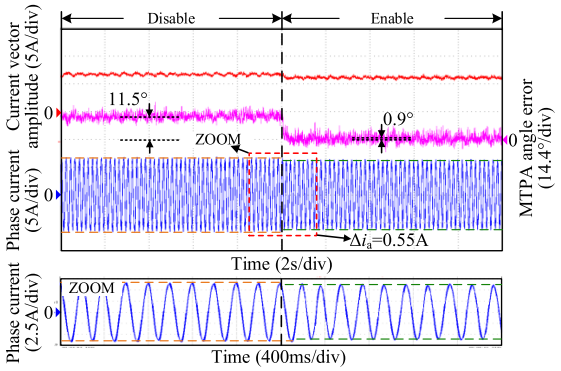

Fig. 15. Experimental results before and after enabling the proposed method.

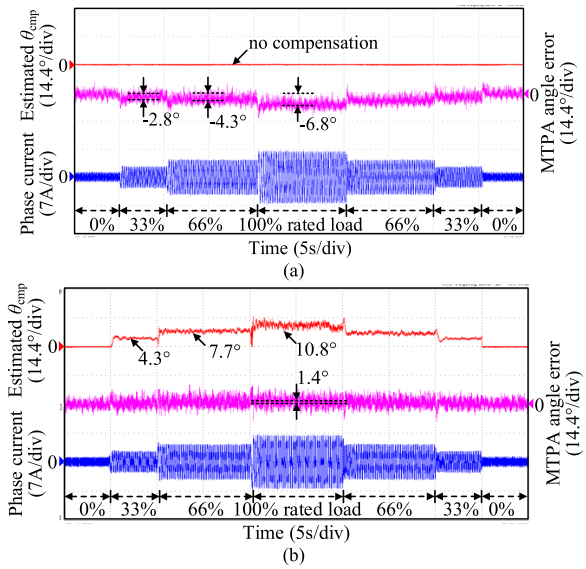

Fig. 16. Experimental results at 100 r/min under continuous load variation conditions. (a) Uncompensated method. (b) Proposed method.

11.5°, including the current vector angle error and the position estimation error due to the cross-saturation effect. After the algorithm is enabled, the MTPA angle error converges to near 0.9°, indicating that the proposed method can accurately track the OCVA in the presence of position estimation error. In addition, the peak phase current is reduced by 0.55 A after the algorithm is enabled, indicating that the proposed method can effectively reduce the current amplitude under the same load condition.

B. Comparisons at Different Loads and Speeds

Fig. 16 shows the experimental results at 100 r/min with continuous load variation conditions. From Fig. 16(a), when the proposed method is not used, the MTPA angle errors are −2.8°, −4.3°, and −6.8° at 33%, 66%, and 100% rated load, respectively. After applying the proposed method, as shown in Fig. 16(b), the MTPA angle error converges to near 1.4° during the load variation, and the MTPA compensation angles are 4.3°, 7.7°, and 10.8°, respectively. From the experimental results, it can be seen that for different loads, the accurate OCVA can be obtained under the position estimation error by using the proposed method.

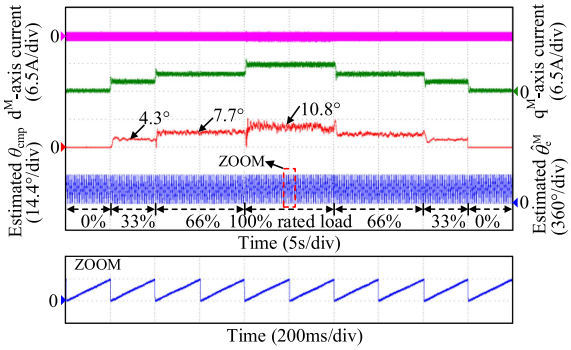

Fig. 17. Experimental results of the intermediate variables at 100 r/min under continuous load variation conditions.

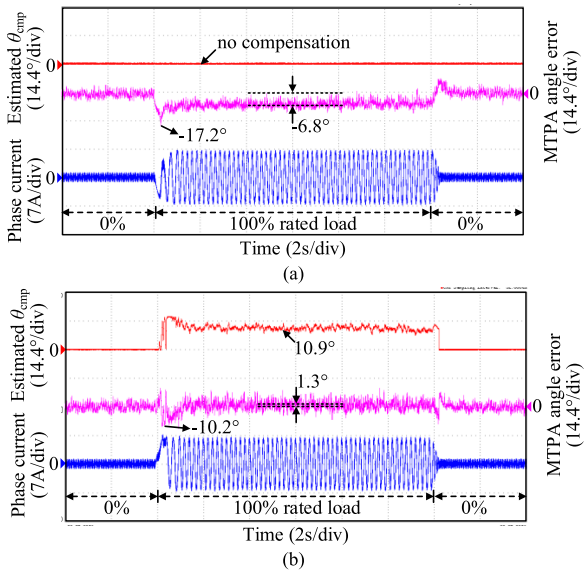

Fig. 18. Experimental results at 100 r/min under sudden load variation conditions. (a) Uncompensated method. (b) Proposed method.

To illustrate the results of Fig. 16(b) more clearly, Fig. 17 shows the waveforms of some intermediate variables in the implementation of the proposed method. As shown in Fig. 17, the $i_d^M = 0$ control is applied in the whole control process, thus the q^M-axis coincides with the current vector. The estimated MTPA compensation angle can be adaptively adjusted as the load varies, thus realizing the tracking of the OCVA under the position estimation error.

To verify the dynamic performance of the proposed method, the experiments of sudden addition and reduction of 100% rated load are carried out at 100 r/min, and the experimental results are shown in Fig. 18. From Fig. 18(a), it can be seen that when the proposed method is not used, the maximum MTPA angle error reaches −17.2° at the moment of sudden load addition, and the steady state MTPA angle error is −6.8°. As shown in Fig. 18(b), the maximum MTPA angle error is −10.2° during sudden load addition after using the proposed method. And then, it takes 0.9 s for the MTPA angle error to converge to near 1.3°. Therefore, the proposed method can still accurately obtain the OCVA during sudden addition and reduction of loads.

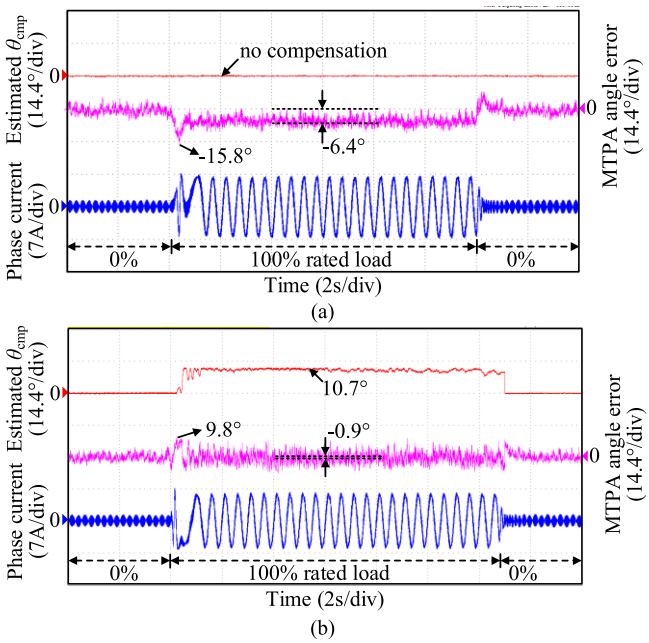

Fig. 19. Experimental results at 40 r/min under sudden load variation conditions. (a) Uncompensated method. (b) Proposed method.

To further validate the dynamic performance of the proposed method at different speeds, Fig. 19 shows the experiment results of the sudden addition and reduction of 100% rated load at 40 r/min. From Fig. 19(a), when the proposed method is not adopted, the maximum MTPA angle error reaches −15.8°, and the steady-state MTPA angle error is −6.4°. After applying the proposed method, as shown in Fig. 19(b), the maximum MTPA angle error is 9.8°, and it finally converges to near −0.9° after 0.8 s.

To verify the performance of the proposed method at very low speeds, the experimental results with load variation conditions at 0 and 2 r/min are given in Fig. 20. From Fig. 20(a), it can be seen that when the proposed method is applied, the MTPA angle error converges to near −2.3° during the load variation at 0 r/min, and the MTPA compensation angles are 5.6°, 9.1°, and 12.9°, respectively. The maximum speed errors are −25, 22, and 22 r/min during the transient process when applying 33%, 66%, and 100% rated load, respectively. What's more, the experimental results with sudden applied loads at 0 r/min are given in Fig. 20(b). From Fig. 20(b), it can be seen that the maximum MTPA angle error is −11.5° and the maximum speed error is 31 r/min during the moment of sudden load addition, and the steady state MTPA angle error is −2.2°. From Fig. 20(c), during the load variation process, the MTPA compensation angles are 3.1°, 7.3°, and 12.3°, respectively. During the transient process, the maximum speed errors are −26, −27, and 24 r/min, respectively. What's more, the experimental results with sudden applied loads at 2 r/min are given in Fig. 20(d). From Fig. 20(d), it can be seen that the maximum MTPA angle error is −9.8° and the maximum speed error is 35 r/min during the moment of sudden load addition, and the steady state MTPA angle error is −1.6°. Therefore, the proposed method can obtain the OCVA at very low speed.

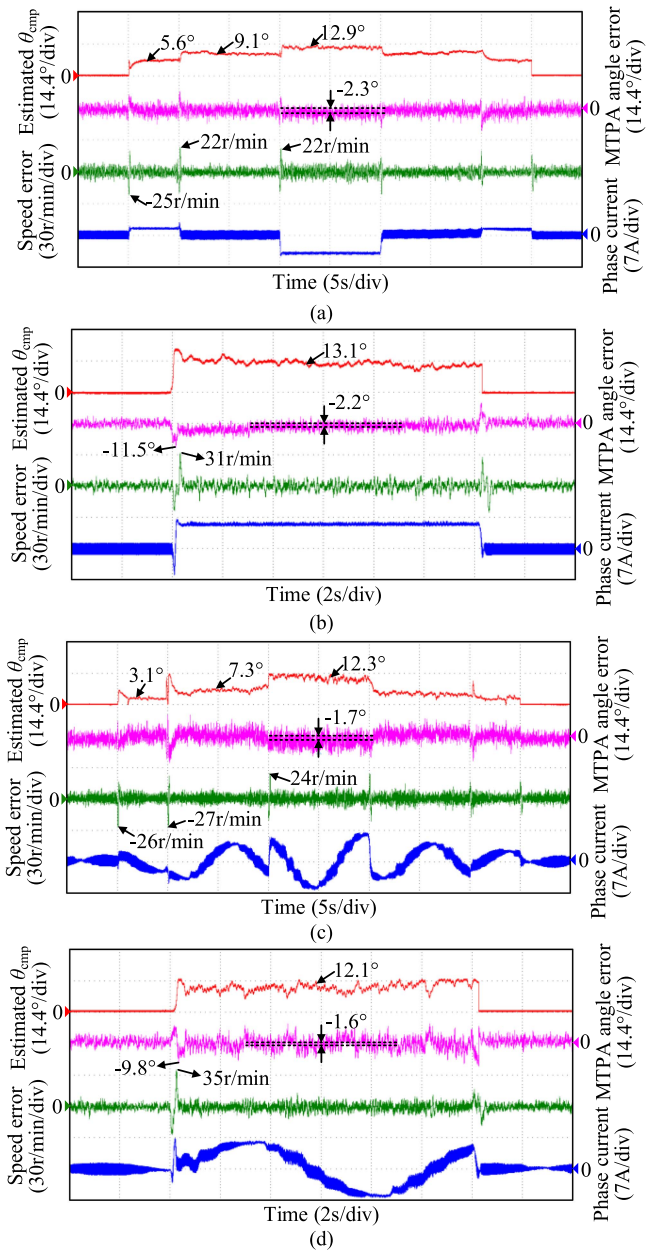

Fig. 20. Experimental results under load variation conditions. (a) Continuous load variation conditions at 0 r/min. (b) Sudden load variation conditions at 0 r/min. (c) Continuous load variation conditions at 2 r/min. (d) Sudden load variation conditions at 2 r/min.

C. Comprehensive Performance Evaluation

To verify the performance of the proposed method, comparative experiments were conducted with the different methods under continuous load variation conditions at 100 r/min. Fig. 21(a) shows the experimental results for the actual signal injection based MTPA control method in [33], revealing a maximum OCVA tracking error of −3.6° under varying loads. What's more, Fig. 21(b) shows the experimental results of the virtual signal injection based MTPA control method considering mutual-induction, with a maximum OCVA tracking error of −3.2°. In contrast, as demonstrated in Fig. 16(b), the proposed

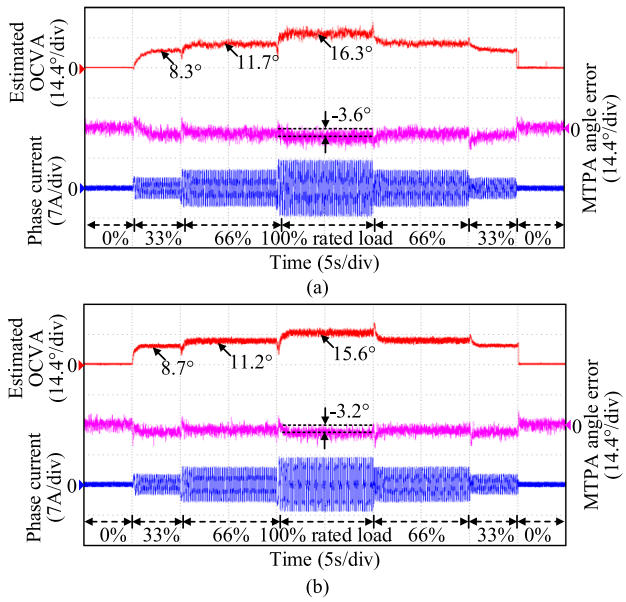

Fig. 21. Experimental results under continuous load variation conditions for different methods. (a) Method in [33]. (b) Method in [15].

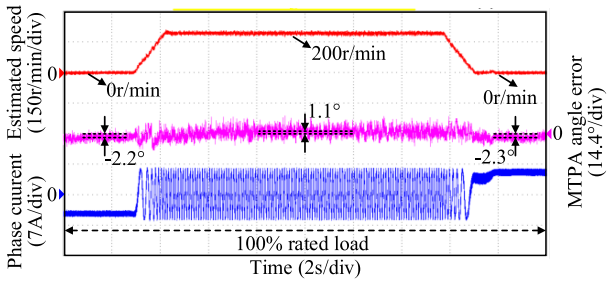

Fig. 22. Experimental results with continuous speed variation conditions.

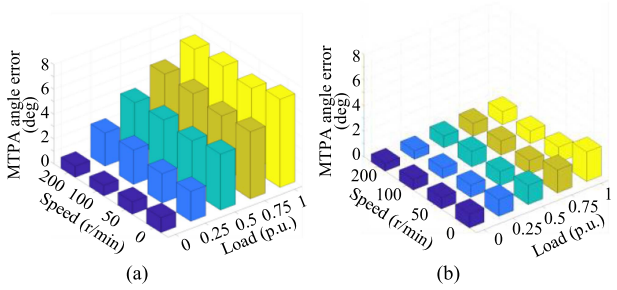

Fig. 23. Comprehensive experimental results of the MTPA angle error under different load and speed conditions. (a) Uncompensated method. (b) Proposed method.

method exhibits a maximum OCVA tracking error of only 1.4° across the same varying load conditions. Therefore, it is evident that the proposed method can improve the OCVA tracking accuracy under the position estimation error.

Fig. 22 shows the experimental results under 100% rated load with continuous speed variation conditions. The motor speed is first stabilized at 0 r/min with 100% rated load, and then the

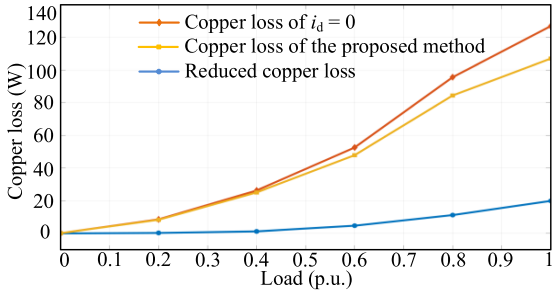

Fig. 24. Copper loss before and after enabling the proposed method.

speed changes from 0 r/min-200 r/min-0 r/min with rated load. From the experimental results in Fig. 22, it can be seen that the steady-state MTPA angle error can be kept within ±3° during the whole acceleration and deceleration process. It can be seen that the proposed method can still obtain the accurate OCVA under continuous speed variation conditions.

Fig. 23 shows the comprehensive experimental results of the MTPA angle error under different load and speed conditions for the proposed method. As can be seen from the results, when the compensation method is not used, the maximum MTPA angle error reaches 7.1° at 0 r/min and 100% rated load. When the proposed method is adopted, the MTPA angle error is effectively suppressed, and the maximum MTPA angle error is 2.3° at 0 r/min and 100% rated load. The MTPA angle error average suppression rate reaches more than 60%.

Fig. 24 shows the copper loss before and after enabling the proposed method at different loads. It can be seen that there is a significant reduction in copper loss at higher loads and a smaller reduction in copper loss at lower loads. Although the proposed method increases the complexity of control, the copper loss is also reduced.

V. Conclusion

In this article, a bi-axis HF sinusoidal injection based sensorless MTPA control method was proposed to improve the MTPA control accuracy. The proposed method established a bi-axis HFSI mechanism in the zero-mutual-inductance and MTPA frames, which achieves the position estimation and OCVA tracking under the position estimation error. The auxiliary HF signal was injected to obtain the accurate estimated frame MTPA criterion, reducing the dependence on the motor parameters. The proposed OCVA tracking error adaptive compensation algorithm realizes the accurate convergence of the MTPA frame under different operating conditions. The stability and parameter selection were analyzed in detail theoretically, which improves the adaptability of the algorithm in complex conditions without a complicated parameter tuning process. The experimental results are consistent with the theoretical analysis, verifying the feasibility and effectiveness of the method, and the average MTPA angle error suppression rate can reach more than 60%. However, the injection of two HF signals may introduce additional torque ripple and HF noise, which will be explored in future work.

REFERENCES

[1] Y. Zuo, C. Lai, and K. L. V. Iyer, "A review of sliding mode observer based sensorless control methods for PMSM drive," *IEEE Trans. Power Electron.*, vol. 38, no. 9, pp. 11352–11367, Sep. 2023.

[2] K. Wang, G. Wang, G. Zhang, Q. Wang, B. Li, and D. Xu, "ESO-based robust hybrid flux observer with active flux error estimation for position sensorless PMa-SynRM drives," *IEEE Trans. Transp. Electrific.*, vol. 11, no. 1, pp. 2049–2060, Feb. 2025.

[3] G. Zhang et al., "Adaptive step-size predictive PLL based rotor position estimation method for sensorless IPMSM drives," *IEEE Trans. Power Electron.*, vol. 39, no. 5, pp. 6136–6147, May 2024.

[4] I. Boldea, A.-A. Popa, and F. Blaabjerg, "Active flux based advanced encoderless AC drives: A tutorial review," *IEEE Trans. Power Electron.*, vol. 39, no. 10, pp. 13510–13523, Oct. 2024.

[5] H. Wang, W. Sun, D. Jiang, and R. Qu, "A MTPA and flux-weakening curve identification method based on physics-informed network without calibration," *IEEE Trans. Power Electron.*, vol. 38, no. 10, pp. 12370–12375, Oct. 2023.

[6] A. Dianov, F. Tinazzi, S. Calligaro, and S. Bolognani, "Review and classification of MTPA control algorithms for synchronous motors," *IEEE Trans. Power Electron.*, vol. 37, no. 4, pp. 3990–4007, Apr. 2022.

[7] X. An, G. Liu, Q. Chen, W. Zhao, and X. Song, "Adjustable model predictive control for IPMSM drives based on online stator inductance identification," *IEEE Trans. Ind. Electron.*, vol. 69, no. 4, pp. 3368–3381, Apr. 2022.

[8] K. Huang, W. Peng, C. Lai, and G. Feng, "Efficient maximum torque per ampere (MTPA) control of interior PMSM using sparse bayesian based offline data-driven model with online magnet temperature compensation," *IEEE Trans. Power Electron.*, vol. 38, no. 4, pp. 5192–5203, Apr. 2023.

[9] G. Feng, C. Lai, X. Tan, and N. C. Kar, "Maximum-torque-per-square-ampere control for interior PMSMs considering cross-saturation inductances," *IEEE Trans. Transp. Electrific.*, vol. 7, no. 3, pp. 1482–1492, Sep. 2021.

[10] T. Sun, L. Long, R. Yang, K. Li, and J. Liang, "Extended virtual signal injection control for MTPA operation of IPMSM drives with online derivative term estimation," *IEEE Trans. Power Electron.*, vol. 36, no. 9, pp. 10602–10611, Sep. 2021.

[11] S. Bolognani, R. Petrella, A. Prearo, and L. Sgarbossa, "Automatic tracking of MTPA trajectory in IPM motor drives based on AC current injection," *IEEE Trans. Ind. Appl.*, vol. 47, no. 1, pp. 105–114, Jan./Feb. 2011.

[12] S. Kim, Y.-D. Yoon, S.-K. Sul, and K. Ide, "Maximum torque per ampere (MTPA) control of an IPM machine based on signal injection considering inductance saturation," *IEEE Trans. Power Electron.*, vol. 28, no. 1, pp. 488–497, Jan. 2013.

[13] G. Liu, Z. Chen, L. Xu, T. Jiang, and L. Chang, "MTPA control for DC-biased hybrid excitation machine using MTPA control law and virtual signal injection," *IEEE Trans. Transp. Electrific.*, vol. 10, no. 1, pp. 1571–1582, Mar. 2024.

[14] H. Wang, C. Li, G. Zhang, Q. Geng, and T. Shi, "Maximum torque per ampere (MTPA) control of IPMSM systems based on controller parameters self-modification," *IEEE Trans. Veh. Technol.*, vol. 69, no. 3, pp. 2613–2620, Mar. 2020.

[15] J. Pang, W. Liu, and N. Jiao, "MTPA control of wound-rotor synchronous start/generator drives based on virtual signal injection considering cross-coupling effect in low-speed range," *IEEE Trans. Power Electron.*, vol. 39, no. 5, pp. 6115–6124, May 2024.

[16] N. Bianchi, E. Fornasiero, and S. Bolognani, "Effect of stator and rotor saturation on sensorless rotor position detection," *IEEE Trans. Ind. Appl.*, vol. 49, no. 3, pp. 1333–1342, May/Jun 2013.

[17] L. Yi, Z. Q. Zhu, D. Howe, C. M. Bingham, and D. A. Stone, "Improved rotor-position estimation by signal injection in brushless AC motors, accounting for cross-coupling magnetic saturation," *IEEE Trans. Ind. Appl.*, vol. 45, no. 5, pp. 1843–1850, Sep./Oct 2009.

[18] D. Q. Dang, M. S. Rafaq, H. H. Choi, and J.-W. Jung, "Online parameter estimation technique for adaptive control applications of interior PM synchronous motor drives," *IEEE Trans. Ind. Electron.*, vol. 63, no. 3, pp. 1438–1449, Mar. 2016.

[19] G. Bi, N. Zhao, G. Zhang, R. Jing, G. Wang, and D. Xu, "Current vector angle adaptive adjustment based rotor position offset error suppression method for sensorless PMSM drives," *IEEE Trans. Power Electron.*, vol. 36, no. 9, pp. 10536–10547, Sep. 2021.

[20] Z. Lin, Q. Geng, Z. Zhou, X. Li, and C. Xia, "MTPA control of sensorless IPMSM based on high frequency square-wave signal injection," in *Proc. IEEE Appl. Power Electron. Conf. Expo.*, 2019, pp. 2577–2581.

[21] Q. Tang, A. Shen, P. Luo, H. Shen, W. Li, and X. He, "IPMSMs sensorless MTPA control based on virtual q-axis inductance by using virtual high-frequency signal injection," *IEEE Trans. Ind. Electron.*, vol. 67, no. 1, pp. 136–146, Jan. 2020.

[22] A. Varatharajan, G. Pellegrino, E. Armando, and M. Hinkkanen, "Sensorless control of synchronous motor drives: Accurate torque estimation and control under parameter errors," *IEEE J. Emerg. Sel. Top. Power Electron.*, vol. 9, no. 5, pp. 5367–5376, Oct. 2021.

[23] J. Yoo, H.-S. Kim, and S.-K. Sul, "MTPA tracking control of sensorless IPMSM based on square-wave voltage signal injection," *IEEE Trans. Power Electron.*, vol. 37, no. 10, pp. 12525–12537, Oct. 2022.

[24] J. Yoo and S.-K. Sul, "Direct MTPA tracking control of sensorless IPMSM in low-speed region," *IEEE Trans. Ind. Electron.*, vol. 72, no. 2, pp. 1271–1280, Feb. 2025.

[25] Q. Tang et al., "Second harmonic seamless splicing technique based on maximum active-voltage vector for online MTPA tracking control of SynRM," *IEEE Trans. Ind. Electron.*, vol. 69, no. 11, pp. 10958–10968, Nov. 2022.

[26] N. Bianchi and S. Bolognani, "Influence of rotor geometry of an IPM motor on sensorless control feasibility," *IEEE Trans. Ind. Appl.*, vol. 43, no. 1, pp. 87–96, Jan./Feb 2007.

[27] Q. Wang, G. Wang, N. Zhao, G. Zhang, Q. Cui, and D. Xu, "An impedance model-based multiparameter identification method of PMSM for both offline and online conditions," *IEEE Trans. Power Electron.*, vol. 36, no. 1, pp. 727–738, Jan. 2021.

[28] S. Liu et al., "Virtual-axis injection based online parameter identification of PMSM considering cross coupling and saturation effects," *IEEE Trans. Power Electron.*, vol. 38, no. 5, pp. 5791–5802, May 2023.

[29] J. Wang et al., "An accurate virtual signal injection control of MTPA for an IPMSM with fast dynamic response," *IEEE Trans. Power Electron.*, vol. 33, no. 9, pp. 7916–7926, Sep. 2018.

[30] G. Zhang, G. Wang, H. Wang, D. Xiao, L. Li, and D. Xu, "Pseudorandom-frequency sinusoidal injection based sensorless IPMSM drives with tolerance for system delays," *IEEE Trans. Power Electron.*, vol. 34, no. 4, pp. 3623–3632, Apr. 2019.

[31] K. Yu and Z. Wang, "Position sensorless control of IPMSM using adjustable frequency setting square-wave voltage injection," *IEEE Trans. Power Electron.*, vol. 37, no. 11, pp. 12973–12979, Nov. 2022.

[32] Q. Tang, A. Shen, X. Luo, and J. Xu, "IPMSM sensorless control by injecting bidirectional rotating HF carrier signals," *IEEE Trans. Power Electron.*, vol. 33, no. 12, pp. 10698–10707, Dec. 2018.

[33] N. Bedetti, S. Calligaro, C. Olsen, and R. Petrella, "Automatic MTPA tracking in IPMSM drives: Loop dynamics, design, and auto-tuning," *IEEE Trans. Ind. Appl.*, vol. 53, no. 5, pp. 4547–4558, Sep./Oct. 2017.

Yunhao Yan received the B.S. degree in electrical engineering in 2023 from the Harbin Institute of Technology (HIT), Harbin, China, where he is currently working toward the Ph.D. degree with the School of Electrical Engineering and Automation.

His current research interests include sensorless control of permanent magnet synchronous motor drives, and MTPA contol.

Guoqiang Zhang (Senior Member, IEEE) received the B.S. degree in electrical engineering from Harbin Engineering University, Harbin, China, in 2011, and the M.S. and Ph.D. degrees in electrical engineering from Harbin Institute of Technology, Harbin, China, in 2013 and 2017, respectively.

Since 2017, he has been with the Department of Electrical Engineering, Harbin Institute of Technology, where he is currently a Professor. His current research interests include control of electrical drives, and parameter identification technique, with main focus on sensorless field-oriented control of synchronous motor drives.

Dr. Zhang is currently an Associate Editor for IEEE TRANSACTIONS ON ENERGY CONVERSION.

Qiwei Wang (Member, IEEE) received the B.S., M.S. and Ph.D. degrees in electrical engineering from the Harbin Institute of Technology, Harbin, China, in 2015, 2017, and 2022, respectively.

He is currently a Postdoctoral in power electronics and electrical drives with the School of Electrical Engineering and Automation, Harbin Institute of Technology. His current research interests include parameter identification technique, and PMSM position sensorless control.

Binxing Li (Member, IEEE) received the B.S. degree in electrical engineering from the Harbin Institute of Technology, Weihai, China, in 2017, and the Ph.D. degree in electrical engineering from the Harbin Institute of Technology, Harbin, China, in 2022.

He is currently a Postdoctor woth School of Electrical Engineering and Automation, Harbin Institute of Technology. His current research interests include permanent magnet synchronous motor drives, high efficiency ac–dc converter, and application of GaN power devices.

Kairan Wang received the B.S. degree in electrical engineering in 2022 from the Harbin Institute of Technology, Harbin, China, where he is currently working toward Ph.D. degree in power electronics and electrical drives.

His current research interests include permanent magnet synchronous motor drives, PMa-SynRM position sensorless control.

Gaolin Wang (Senior Member, IEEE) received the B.S., M.S., and Ph.D. degrees in electrical engineering from Harbin Institute of Technology, Harbin, China, in 2002, 2004, and 2008, respectively.

In 2009, he was a Lecturer with the Department of Electrical Engineering, Harbin Institute of Technology, where he has been a Full Professor of electrical engineering since 2014. From 2009 to 2012, he was a Postdoctoral Fellow with Shanghai Step Electric Corporation, where he was involved in the traction machine control for direct-drive elevators. He has authored more than 70 technical papers published in IEEE Transactions. He is the holder of 40 Chinese patents. His current major research interests include permanent magnet synchronous motor drives, position sensorless control of ac motors, and digital control of power converters.

Dr. Wang is currently a Guest Associate Editor for IEEE TRANSACTIONS ON INDUSTRIAL ELECTRONICS, an Associate Editor for IEEE TRANSACTIONS ON TRANSPORTATION ELECTRIFICATION, *IET Electric Power Applications*, and *Journal of Power Electronics.*

Dianguo Xu (Fellow, IEEE) received the B.S. degree in control engineering from the Harbin Engineering University, Harbin, China, in 1982, and the M.S. and Ph.D. degrees in electrical engineering from the Harbin Institute of Technology (HIT), Harbin, China, in 1984 and 1989, respectively.

In 1984, he was with the Department of Electrical Engineering, HIT, as an Assistant Professor. Since 1994, he has been a Professor with the Department of Electrical Engineering, HIT. He was the Dean of the School of Electrical Engineering and Automation, HIT, from 2000 to 2010, and an Assistant President from 2010 to 2014. He is currently the Vice President with HIT. He authored or co-authored more than 600 technical papers. His research interests include renewable energy generation technology, power quality mitigation, sensorless vector-controlled motor drives, high-performance PMSM servo system.

Dr. Xu is the Co-EIC for IEEE TRANSACTIONS ON POWER ELECTRONICS, an Associate Editor of IEEE TRANSACTIONS ON INDUSTRIAL ELECTRONICS, IEEE JOURNAL OF EMERGING AND SELECTED TOPICS IN POWER ELECTRONICS. He was the recipient of the 2018 IEEE IAS Outstanding Achievement Award.